Toxic Gas Sensors using Thin Film Transistor Platform at Low Temperature

by

Yoonsil Jin

B.S. Materials Science and Engineering
Hanyang University, 2004

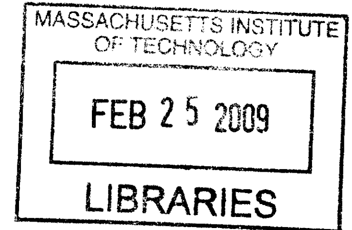

Submitted to the Department of Materials Science and Engineering in Partial Fulfillment of the Requirements for the Degree of

Master of Science in Materials Science and Engineering
at the

Massachusetts Institute of Technology

February 2009

©2009 Massachusetts Institute of Technology
All rights reserved.

Signature of Author: ______________
Department of Materials Science and Engineering
January 30, 2009

Certified by: ______________
Harry L. Tuller
Professor of Ceramics and Electronic Materials
Thesis supervisor

Accepted by: ______________
Christine Ortiz
Associate Professor of Materials Science and Engineering
Chair, Departmental Committee on Graduate Students

ARCHIVES

Toxic Gas Sensors using Thin Film Transistor Platform at Low Temperature

by

Yoonsil Jin

Submitted to the Department of Materials Science and Engineering on January 23, 2009 in Partial Fulfillment of the Requirements for the Degree of Master of Science in Materials Science and Engineering

ABSTRACT

Semiconducting metal-oxides such as SnO_2, TiO_2, ZnO and WO_3 are commonly used for gas sensing in the form of thin film resistors (TFRs) given their high sensitivity to many vapor species, simple construction and capability for miniaturization. Furthermore, they are generally more stable than polymer-based gas sensors. However, unlike polymers, metal oxide gas sensors must typically be operated between 200-400°C to insure rapid kinetics. Another problem impacting TFR performance and reproducibility is related to poorly understood substrate-semiconductor film interactions. Space charges at this heterojunction are believed to influence chemisorption on the semiconductor-gas interface, but unfortunately, in an unpredictable manner.

In this study, the feasibility of employing illumination and the thin film transistor (TFT) platform as a means of reducing operation temperature was investigated on ZnO based TFTs for gas sensors applications. Response to NO_2 is observed at significantly reduced temperature. Photoconductivity measurements, performed as a function of temperature on ZnO based TFRs, indicate that this results in a photon-induced desorption process. Also, transient changes in TFT channel conductance and transistor threshold voltage are obtained with application of gate bias, suggesting that TFTs offer additional control over chemisorption at the semiconductor-gas interface.

Thesis Supervisor: Harry L. Tuller

Title: Professor of Ceramics and Electronic Materials

Acknowledgements

First of all, I would like to express my special gratitude to my thesis advisor, Professor Harry L. Tuller, for his insightful guidance and patience over the years. I deeply appreciate him for taking time out of his busy schedule to provide me his time and input. Without his encouragement, this thesis would never been accomplished.

I would also thank the other members of our group including George, Scott, Woochul and Kengo for their friendship beyond technical discussions. Special thanks to my friends here at MIT, Seungeun, Suh-Kyung and Hyun Jung for making my life enjoyable.

I am grateful to Dr. Il-Doo Kim at Korea Institute of Science and Technology for providing me with the thin film transistors

Most importantly, I would like to thank my mother, sisters and brother who were always there for me along the way. I cannot thank them enough for their endless love and belief in me.

TABLE OF CONTENTS

Abstract 2

Acknowledgements...3

Table of Contents...4

List of Figures..6

List of Tables..9

1. **Introduction**...10

2. **Background**..12

2.1. **Semiconducting metal oxide gas sensor**....................................12

2.1.1. Sensing mechanism of bulk-type metal oxide gas sensors..................12

2.1.2. Sensing mechanism of interfacial-type metal oxide gas sensors.............14

2.1.3. Sensor requirements and characteristics...17

2.2. **Thin-film transistor gas sensor**..18

2.2.1. Thin-film metal oxide gas sensors..18

2.2.2. Characteristics of thin film transistor..21

2.2.3. Physics of thin film transistor..22

2.2.4. Volkenstein theory

2.3. **$InGaZnO_4$**..27

2.3.1. Transparent oxide semiconductors..27

2.3.2. Amorphous $InGaZnO_4$...28

2.3.3. Electron transport in ionic amorphous oxide semiconductors................30

3. **Experimental procedure**....................33
3.1. Model system....................33
3.2. Electrical measurements for gas sensor measurements....................35

4. **Results**....................37
4.1. Sensor performance at reduced temperature....................37
4.2. Conductance measurement under illumination....................39
4.3. Field effect on electrical characteristics of $IGZO_4$ thin film transistor....................44
4.3.1. Threshold voltage measurement of a $IGZO_4$ TFT....................44
4.3.2. Transient conductance measurement of $IGZO_4$ TFT under field effect...46
4.3.3. Transient conductance under negative bias at different temperatures.......51
4.4. Conductance measurement under both illumination and field effect....................53

5. **Discussion**....................56
5.1. Enhanced chemisorption kinetics of amorphous IGZO....................56
5.2. The influence of illumination on chemisorption at semiconductor/gas interfaces
....................58
5.3. The influence of field effect on chemisorption at semiconductor/gas interfaces
....................62
6. **Summary and future work**....................68
Reference

List of Figures

Figure

1. Equilibrium conductivity of $BaTiO_3$ as a function of oxygen partial pressure at temperatures from 600 to 1000^{0}C....................14
2. Schematic presentation of the effect of the ambient gas atmosphere on the energy band diagram of an n-type metal-oxide in clean air (a); reducing gases in air (b); and oxidizing gases in air (c)....................16
3. Schematics of a compact sensing layer geometry and energy band; z_0 is the thickness of the depleted surface layer, z_g is the layer thickness and qV_s the is band bending. (a) A partly depleted compact layer ("thicker") (b) A completely depleted layer (thinner)....................19
4. Schematic of a porous sensing layer with geometry and surface energy band with necks between grains; x_o is the length a depletion layer, λ_D is the debye length and x_g is grain size (a) large grains (b) small grains....................20
5. Characteristic curves of a thin film transistor. a) General output characteristics of TFT; (b) General form of transfer characteristics for V_{DS}=5 V. The graph shows extraction of threshold voltage V_{TH} by plotting $I_{DS}^{1/2}$ and V_{GS}....................22
6. a) Cross-sections of a conventional n-channel MOSFET; b) Energy band diagram for an n-channel MOS under strong inversion, $V_{GS} > V_{TH}$. S: source electrode, G: gate electrode, D: drain electrode....................23
7. a) Cross- section of an n-channel thin-film field effect transistor; b) Energy band diagram for an n-channel TFT under large positive gate bias, resulting in formation of an electron channel....................23
8. Energy band diagrams for MOS capacitors with a thin semiconducting layer, where $t_s < \lambda$....................24
9. (a) Energy band diagram of a semiconductor with chemisorbed molecules (denoted A). (b) Relative change in the adsorptive capacity $\frac{\Delta N}{N_{V_{GS}=0V}}$ of the surface of an n-type semiconductor as a function of applied bias via electrode.................... 26
10. The amorphous formation region in the In_2O_3-Ga_2O_3-ZnO system (left) and the electron mobilities and carrier concentrations (right) evaluated from the Hall effect

for amorphous thin films in the In_2O_3-Ga_2O_3-ZnO system [38]. The thin films were deposited on a glass substrate by pulsed laser deposition under the atmosphere of Po_2=1Pa. Numbers in parenthesis denote carrier electron concentration ($x10^{18}cm^{-3}$) 29

11. XRD pattern of a-IGZO film deposited on SiO_2 glass substrate by PLD..............30
12. Structure of single crystalline $IGZO_4$. (left) LDA-relaxed structure of amorphous $IGZO_4$ containing $(InGaZnO_4)_{12}$ atoms. (right) MO_n (M=metal cation, n=integer) indicates a specific coordination structure with MO_n polyhedra.......................30
13. Comparison of energy bandgap formation between (a) covalent semiconductor and (c) ionic semiconductor ($M^{2+}O^{2-}$)...31
14. Schematic illustration of orbitals in (a) crystalline and (b) amorphous structures of ionic oxide semiconductors. This image is valid for oxides of heavy metal cations with $(n-1)d^{10}ns^0$ ($n \geq 5$) configuration...32
15. (a) Schematic of IGZO TFTs on a heavily p-type silicon substrate. (b) The top view image of TFTs placed inside of a custom-designed microprobe station. Numbers in (a) denotes the channel lengths and widths of TFTs.......................................33
16. (a) Schematic of cross-sectional view of the a-IGZO TFT structure. (b) Top view of IGZO TFT..34
17. (a) A schematic of gas sensor measurement set-up (b) A real image of the custom-designed microprobe station...35
18. Sensor response of IGZO films to 10ppm NO_2 in synthetic air (50% R.H., 25^{0}C at different temperatures; room temperature, 60^{0}C and 100^{0}C...........................37
19. Temperature dependent sensitivity of IGZO thin film to 10 ppm NO_2 in synthetic air (50% R.H., 25^{0}C)...38
20. Temperature dependence of conductance (a) under synthetic air (b) under 10ppm NO_2 in synthetic air...38
21. The channel conductance of an a-$IGZO_4$ thin film operating in a 100% oxygen atmosphere. The broad band light source is turned on and off according to the above figure..40

22. The channel conductance under the influence of 10 ppm NO_2/Air measured at room temperature. The broad band light source is turned on and off according to the above figure..41
23. The effect of gate bias on (a) threshold voltage V_{TH} of a $IGZO_4$ TFT exposed to 100 ppm NO in N_2 (b) Applied gate bias V_{GS} as a function of time........,,,,,,,,,,,,,,.....45
24. (a) Conductance changes of a-IGZO thin film under the influence of 100% oxygen upon gate bias application (b) Applied gate bias versus time. Successively higher magnitude negative or positive biases are applied alternating with 0 V..................48
25. (a) Conductance changes of a-IGZO thin film under high vacuum upon gate bias application (b) Applied gate bias versus time. Successively higher magnitude negative or positive biases are applied alternating with 0 V..........................49
26. (a) Conductance changes of a-IGZO thin film under 50 ppm NO/N_2 upon gate bias application, (b) Applied gate bias versus time. Negative or positive biases, $\pm 5V, \pm 10V \cdot and \pm 15V$, are applied over successively increasing times alternating with 0 V...50
27. Conductance upon negative gate bias (V_{GS}) applications under a 50 ppm NO in N_2 atmosphere as a function of temperature. V_{GS}= -10V is applied for 5 hours at different temperatures; Room temperature, 100^{0}C, 150^{0}C. V_{GS} = 0V is held prior to and following negative gate bias applications...51
28. Channel conductance of IGZO TFT when the gate bias and broad band illumination are applied under 50 ppm NO/N_2 environments (a). Applied gate bias vs time (b). 54
29. Energy band diagram of photon-induced desorption upon band-gap irradiation for an n-type semiconductor. Gray area represents states or band populated with electrons..60
30. A schematic of an energy band diagram of TFT exposed to oxidizing gases.........64
31. Schematics of energy band diagram during field-induced adsorption. TFTs are (a) under positive gate bias V_{GS} >V_{TH} (b) after field induced-adsorption. 65
32. Schematics of energy band diagram of TFT during field induced-desorption. TFTs are under (a) negative gate bias and (b) after the field-induced desorption...65

List of Tables

Table

1. Key components of the IGZO TFT..34
2. Test gases for electrical measurements..36
3. Annealing procedure followed prior to sensor characterization...........................40
4. Time constants for oxygen desorption and re-adsorption on IGZO film...................42
5. Time constants for NO_2 desorption and re-adsorption on IGZO film at room temperature...43
6. Time constants for field-induced desorption at various temperatures.....................52
7. Applied gate voltages and its effect on chemisorption....................................67

1. Introduction

The demand for better chemical sensors is ever increasing in many applications, including automotive cabin air quality control,[1] hazardous (explosive/toxic) gas alarms,[2,3] process control (food and cosmetics industries)[4,5,6] , medical diagnosis[7,8] and feedback control systems. To meet these needs, sensors need to exhibit high sensitivity and selectivity, stability, rapid response and recovery times at reasonable cost. Besides, low power consumption and miniaturization, other desirable features such as device portability are becoming important.

At present, three major types of solid-state gas sensors have been commercialized in large-scale use[9]: potentiometric sensors based on solid electrolytes, pellistors based on catalytic combustion and resistive sensors based on semiconducting metal oxides such as SnO_2, TiO_2, ZnO and WO_3. Among various types of gas sensors, metal-oxide gas sensors (MOGSs) offer many advantages over alternative solid-state gas sensor devices: high sensitivity, low cost, the ready ability to integrate in micro-arrays and simple design and operation. However, due to the non-specificity of the chemical interactions that eventually lead to their response signal, MOGSs suffer from relatively poor selectivity that inhibits their widespread application.[10,11] Secondly, MOGSs typically need to be heated to temperatures between 200-400°C to insure sufficiently rapid kinetics. This requirement, i.e. high operation temperature of MOGSs often leads to several problems: high power consumption for heating, reduced sensitivity and selectivity and degradation over time. Thus, if one can obtain sufficiently rapid kinetics at relatively reduced operation temperature, the performance of current MOGSs can be significantly improved. In this thesis, several approaches are investigated to realize low temperature operation of MOGSs including: use of novel semiconducting metal oxides (SMO), illumination and the field effect.

A novel semiconducting metal oxide (SMO), $InGaZnO_4$ (IGZO), introduced by Nomura et al., has attracted considerable attention by researchers and scientists due to its high electron mobility (~10 $cm^2/Vsec$) even in amorphous form. While most of the research on IGZO is focused in its use as transparent thin film transistors (TFT), recent observations by Kang et. al.[12] suggested IGZO as a possible sensor material at low temperature given its

strong response to oxygen partial pressure variation, even at ambient temperature. They reported a turn-on voltage shift for IGZO TFTs from -7 to -54V as the pressure in the chamber decreased from 760 to $8.5x10^{-6}$ Torr, and a return to the initial voltage upon re-exposure to air. The oxygen adsorption and desorprtion processes are assumed to be the main source of this marked shift in turn-on voltage. This hypothesis is supported by a decrease in work function (WF) during a 1300 minute vacuum anneal; also indicating a sluggish oxygen desorption process consistent with observations by Lagowski et al[13]. There have been a few studies[14,15] on GasFETs which expose the semiconducting metal oxide channel to the gas atmosphere and simultaneously manipulate the gate bias to influence sensor performance. However, these have been operated at elevated temperatures leading to unstable operation. Below, we emphasize the utility of the **thin film transistor (TFT)** in serving as an ideal platform for the **thin film resistor (TFR)** by enabling systematic control of such substrate effects.

2. Background

2.1. Semiconducting metal oxide gas sensor

2.1.1. Sensing mechanism of bulk-type metal oxide gas sensors

Highly sensitive oxygen sensors are required to monitor the air to fuel ratios of exhaust gases from internal combustion engines, especially under lean-burn conditions, for which conventional potentiometric gas sensors are limited in their performance. The bulk type of semiconducting metal oxide gas sensors are employed in this application given their high sensitivity. The well-known relationship between electrical conductivity, σ , and oxygen partial pressure are given by equation (2.1)

$$\sigma = \sigma_0 \exp(-E_A / kT) P_{O_2}^{\ 1/n} \qquad (2.1)$$

where E_A denotes an activation energy of bulk conduction, P_{O_2} is the oxygen partial pressure and the value and sign of n is determined by the dominant type of bulk defect.

At elevated temperatures, 700°C and above, semiconducting metal oxides readily deviate from stoichiometry by generating ionic defects and electronic charge carriers to maintain equilibrium between oxygen in the atmosphere and oxygen in the metal oxides. This is reflected as an electronic conductivity change which can be measured. Semiconducting metal oxides such as TiO_2, $BaTiO_3$ and $SrTiO_3$ are heavily investigated as high temperature oxygen sensors.

For a more detailed explanation of equation (2.1), TiO_2, the first material investigated for this purpose, will be taken as an example. When TiO_2 is exposed to a low oxygen partial pressure environment, at high enough temperature to equilibrate, 4-fold ionized Ti interstitials, $Ti_i^{\bullet\bullet\bullet\bullet}$, are believed to form. This reduction reaction is expressed by equation (2.2)

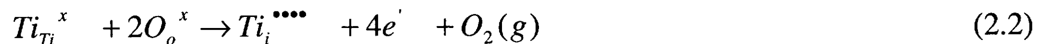

$$Ti_{Ti}^{\ x} + 2O_o^{\ x} \rightarrow Ti_i^{\bullet\bullet\bullet\bullet} + 4e' + O_2(g) \qquad (2.2)$$

where the equilibrium constant of the reaction is given by equation (2.3).

$$K_R = [Ti_i^{\bullet\bullet\bullet\bullet}] \cdot n^4 \cdot P_{o_2} \tag{2.3}$$

Given the charge neutrality equation as equation (2.4),

$$4 \cdot [Ti_i^{\bullet\bullet\bullet\bullet}] = n \tag{2.4}$$

The electron concentration, n, is obtained by combining equation (2.3) and (2.4).

$$n = 4 \cdot [Ti_i^{\bullet\bullet\bullet\bullet}] = (4K_R)^{1/5} \cdot (P_{O_2})^{-1/5} \tag{2.5}$$

Considering that the electronic conductivity is defined by $\sigma = ne\mu$, the dependence of the electronic conductivity on oxygen partial pressure, given by equation (2.1), is easily understood.

One obvious difficulty of utilizing bulk type semiconducting metal oxide gas sensors can be deduced by considering equation (2.1). Since the electrical conductivity depends not only on oxygen partial pressure but also on temperatures, considerable uncertainty in the sensor response will be introduced unless the temperature is held constant. To overcome this problem, two engineering solutions were initially proposed: either the operation temperature of the sensors is held constant above that of the exhaust gas by a built-in heater; or temperature variations in the device are compensated by measuring a response from a dense TiO_2 reference which operates at the same temperature with that of porous TiO_2, but cannot change its stoichiometry in the short times required for sensor operation[16].

An alternative solution would be to employ materials which have a nearly zero activation energy, which in turn leads to a significantly reduced temperature dependence of conductivity. By employing these kinds of materials, oxygen sensors can be constructed without need for additional temperature control or compensation elements. A family of doped perovskite structure oxides such as $BaFe_{0.8}Ta_{0.2}O_3$ has been found to have a nearly zero activation energy over a wide temperature range. Figure 1 shows the electrical

conductivity of $BaTiO_3$ as a function of oxygen partial pressure at various temperatures. An important feature, i.e. small activation energy, is manifested in the p-type range where isothermal lines are very much closer together than in the n-type range. This is because the effects on conductivity of thermal generation of charge carriers and stoichiometric deviations cancel each other[9].

2.1.2. Sensing mechanism of interfacial-type metal oxide gas sensors

Minor concentrations of toxic or combustible gases can also be detected with semiconducing metal oxide gas sensors. For this application, a porous semiconducting metal oxide, usually SnO_2, is used and the operation temperature is maintained in the range of 300~500°C. Considering the relatively fixed oxygen partial pressure (0.2 atm) and the low operating temperature which does not allow for bulk diffusion to occur, it is obvious that the mechanism appropriate for bulk conductivity change is not relevant for this application.

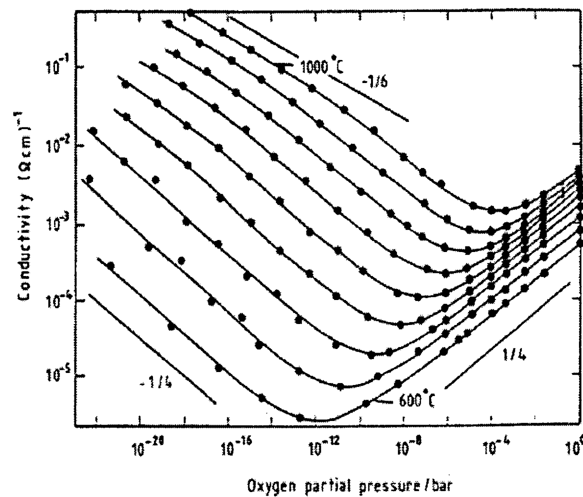

Figure 1. Equilibrium conductivity of $BaTiO_3$ as a function of oxygen partial pressure at temperatures from 600 to 1000°C. A transistion from n-type to p-type behavior occurs with increasing oxygen partial pressure. From P T Moseley, Meas. Sci. Technol. 8 (1997)

The sensing mechanism of this type of sensor involves changes in the density of charge carriers at the semiconductor/ gas interface induced by charge transfer interactions

with adsorbed gases. These surface reactions are eventually manifested as changes in electrical conductivity of the metal oxide films. A more detailed explanation will be described below in case of an n-type semiconducting metal-oxide.

Initially, oxygen from the ambient atmosphere adsorbs on the surface and captures an electron from the conduction band to produce a chemisorbed oxygen adion, $O^-_{(ad)}$ with surface charge density $N_s^- = \lfloor O^-_{(ad)} \rfloor$ [17] through the reaction given by equation (2.6).

$$\tfrac{1}{2}O_{2(g)} + e^-_{cb} \leftrightarrow O^-_{(ad)} \qquad (2.6)$$

As a result, the surface becomes negatively charged and the energy bands bend upwards, creating a surface potential barrier as shown in Figure 2(a). The surface depletion width W is defined by equation (2.7a), determining the initial resistance of the metal oxide in air. Here, N_D is the number of ionized donor states per unit volume and K, ε_0, $\Delta\phi_s$ denote the static dielectric constant of the oxide, the permittivity of vacuum, and the surface potential barrier height, respectively.

$$W = \frac{N_s^-}{e \cdot N_D} = \left[\frac{2 \cdot K \cdot \varepsilon_0 \cdot \Delta\phi_s}{e \cdot N_D}\right]^{1/2} \qquad (2.7a)$$

Exposure to reducing gases $(Re_{(g)})$ such as CO, H_2, and CH_4, decreases the surface state density because these gases interact with pre-adsorbed oxygen adions and remove them from the surface by the reaction expressed in equation (2.7b)17 .Consequently, the energy bands bend downwards, and the surface depletion layer becomes narrower (with respect to the situation in air), as shown in Figure 2(b). Thus, the resistance of n-type metal oxides will decrease upon exposure to reducing gases, as surface coverage of adsorbed oxygen is decreased.

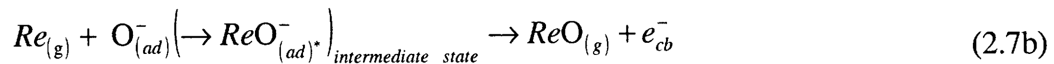

$$Re_{(g)} + O^-_{(ad)} \left(\rightarrow ReO^-_{(ad)^*}\right)_{intermediate\ state} \rightarrow ReO_{(g)} + e^-_{cb} \qquad (2.7b)$$

In contrast, exposure to oxidizing gases such as NO_x or Cl_2 increases the surface charge density, $N_s^- = [O^-_{(ad)}] + [Ox^-_{(ad)}]$, because these strong oxidizing agents capture more electrons from the conduction band by the reaction expressed in equation (2.8).

$$Ox_{(g)} + e^-_{cb} \rightarrow Ox^-_{(ad)} \tag{2.8}$$

As a result, the surface region becomes even more depleted of carriers, the energy bands bend upwards, and the depletion region extends deeper into the bulk, as shown in Figure 2(c). Therefore, the resistance of the metal oxide will increase.

To summarize, the surface charge density increases with increasing concentrations of oxidizing gases and decreases with increasing concentrations of reducing gases. In n-type gas sensors, increases in conductivity indicate exposure to reducing gases whereas decreases in conductivity indicate exposure to oxidizing gases. However, the situation is reversed for gas sensors made of p-type metal-oxides, which are less common than n-type sensors. Since the charge carriers in p-type metal oxides are holes, the conductivity will increase as adsorbed oxygen removes electron from valence band and hence giving rise to an increase in hole concentration.

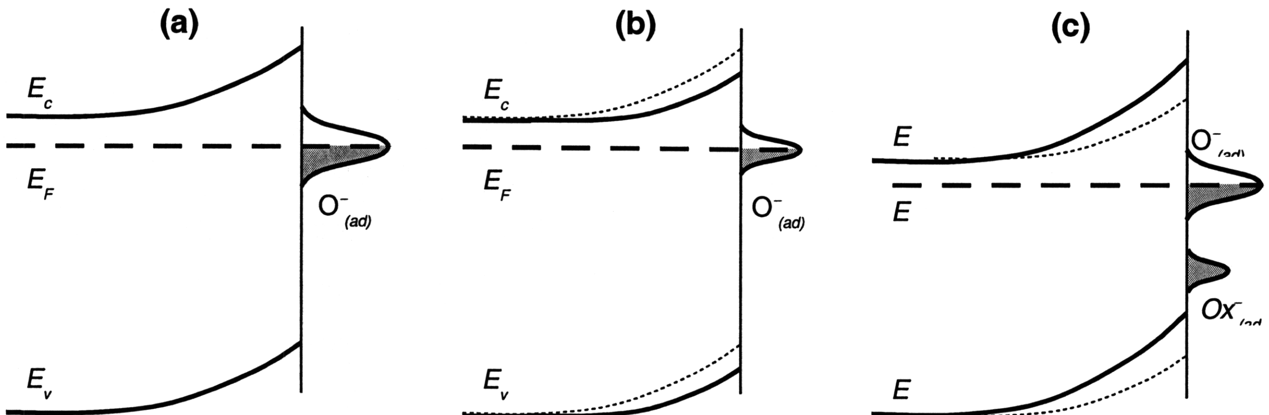

Figure 2. Schematic presentation of the effect of the ambient gas atmosphere on the energy band diagram of an n-type metal-oxide in clean air (a); reducing gases in air (b); and oxidizing gases in air (c).

Based on the statements made above, one can readily grasp the origin of non-selectivity that metal oxide gas sensors possess. In an uncontrolled gas atmosphere, where

various reducing and oxidizing gases could be present at different concentrations, one cannot easily distinguish between different gases belonging to the same group (oxidizing or reducing gases) unless the sensor is made selective to a specific gas.

2.1.3. Sensor requirements and characteristics

In order to be used in practice, a gas sensor should satisfy many requirements depending on the purposes and conditions of sensor operation. The key requirements of chemical sensors can be divided into two category; sensing performance–related ones (e.g., sensitivity, selectivity and response time) and reliability-related ones (e.g., drift, stability and poisoning)[18]. In addition, small size (portability), simple operation, simple fabrication and low manufacturing cost and low power consumption (i.e., low operation temperature) are required for successful commercialization of gas sensors. Here, only some of the key characteristics will be defined: sensitivity, selectivity, response time and recovery time.

First, the *sensitivity* is defined as follows for a given concentration of gas in case

$$Sensitivity = \frac{\Delta G = G_{reducing\ gas} - G_{air}}{G_{air}} \quad or \quad \frac{\Delta R = R_{oxidizing\ gas} - R_{air}}{R_{air}} \tag{2.9}$$

of n-type metal oxides where subscripts of conductance (G) and resistance (R) denote the type of gases of interest[19] . Alternatively, the sensitivity is simply defined as $\frac{R_{Air}}{R_{Reducing\ gas}}$ $or \frac{R_{oxidizing\ gas}}{R_{Air}}$ for n-type metal oxides for convenience. The efforts to improve the sensitivity of metal oxides have been made vigorously owing to recent demands for detection of harmful gases and odors with sub-ppm levels. Nanocrystalline and thin film metal oxides gas sensors are typical example of these efforts.

In general, the *selectivity* is defined as $\frac{Sensitivity\ to\ gas1}{Sensitivity\ to\ gas2}$ for equivalent concentration of both gases[18]. Metal oxide gas sensors are known to exhibit poor selectivity due to the

inherent non-selective nature of the sensing mechanism as discussed in the previous section. Recently, efforts to overcome this problem have been made by employing sensor arrays which utilize pattern recognition techniques[20].

The *response time* is normally defined as the time taken to reach 90% of the final change in conductance (or resistance) upon the change of gas concentration. However, response times are often expressed as 50% or 70% of the time taken to reach the final value in resistance since long and sluggish response is followed by fast initial response before reaching a steady value. The response time is an important parameter since it determines the applicability of the sensor. For example, the order of a few milliseconds is desirable for monitoring exhaust gases from internal combustion. In order to obtain rapid response times, metal oxide gas sensors are normally heated to elevated temperature to aid charge transfer associated with chemisorption processes.

The *recovery time,* likewise, is the time a sensor takes to recover to its initial resistance or conductance once the gas of interest is removed from the gas stream which is normally air. However, recovery times are frequently expressed as time taken to reach 70% or 90% of its initial resistance or conductance.

2.2. **Thin-film transistor gas sensor**

2.2.1. Thin film metal oxide gas sensor

Before delving into topics related to thin film transistor gas sensors, the conduction model of thin film metal oxide gas sensors will first be described as it lays the basis of understanding of phenomena involved in the detection process.

The thin film metal oxide gas sensor usually consists of a sensitive layer, i.e. metal oxide thin film, electrodes, heater and substrate. In general, two conduction models are suggested depending on the sensing layer morphologies: compact vs porous.

The compact layers can be obtained with most thin film deposition techniques such as pulsed laser deposition, sputtering etc. As illustrated in Figure 3, gases only interact with metal oxides at geometrical surfaces in the case of compact layers, resulting in a surface depletion layer through the film either partly (a) or completely (b). Whether the sensor

operates under a partly or a completely depleted condition is determined by the ratio between layer thickness z_g and Debye length λ_D .

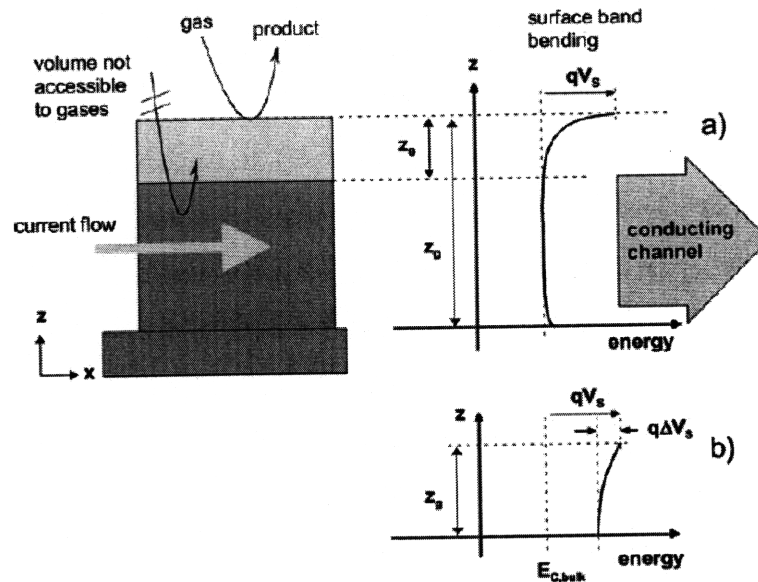

Figure 3. Schematics of a compact sensing layer geometry and energy band; z_0 is the thickness of the depleted surface layer, z_g is the layer thickness and qV_s is the band bending. (a) A partly depleted compact layer ("thicker") (b) A completely depleted layer (thinner)

Since conduction is parallel to the surface in this case, this type of sensor exhibits limited sensitivity. For completely depleted layers, exposure to reducing or oxidizing gases can act as a switch between completely depleted and partly depleted layers depending on the initial state of the sensing film.

Figure 4 illustrates the conduction model of a porous sensing layer with geometry and surface energy band for small and large grains. For large grains, conduction can be hindered by the formation of depletion layers at surface/bulk regions and grain boundaries; the presence of energy barriers blocks the motion of charge carriers. In contrast, flat band conditions dominate in case of small grains, allowing fast conduction for this case.

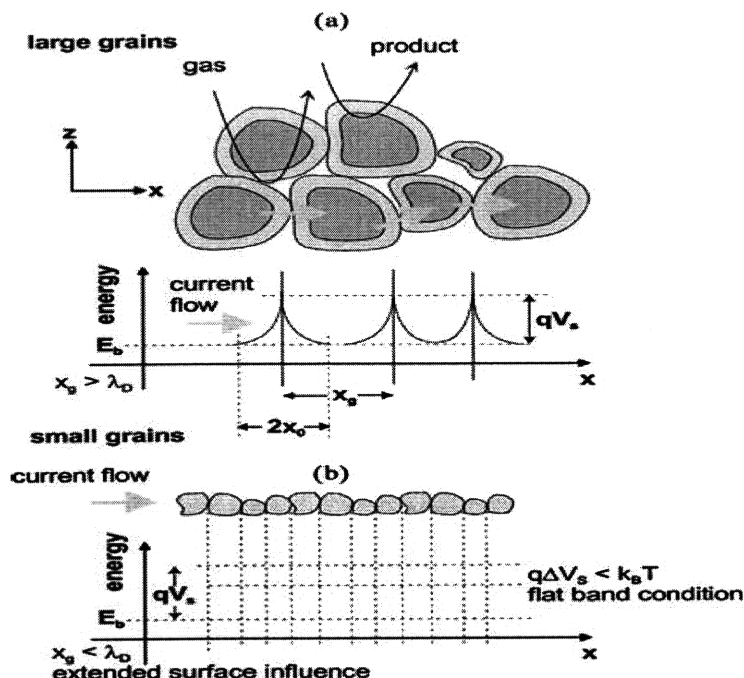

Figure 4. Schematic of a porous sensing layer with geometry and surface energy band with necks between grains; x_o is the length a depletion layer, λ_D is the debye length and x_g is grain size (a) large grains (b) small grains

While metal oxide gas sensors based on the thin film resistor (TFR) can be quite sensitive, the gas sensing characteristics of TFRs remain difficult to reproduce, due to space charge effects at the SMO film-substrate interface.[21] For thin enough films, space charge effects at this interface can markedly influence band bending at the SMO-gas interface and, in turn, gas sensitivity. Since little or no effort has been made to control and/ or characterize the SMO film-substrate heterojunction, it is therefore not surprising that TFRs often exhibit irreproducible sensor responses. In order to a) reproducibly control space charge and band bending at the SMO film-substrate interface and b) use this control to optimize sensor sensitivity, selectivity and response time, I have selected the *Buried Gate TFT Structure* as a model platform for performing studies and testing. With the assistance of illumination and/or choice of novel SMOs, studies in this thesis can be restricted to at or near ambient temperatures, thereby eliminating a key source of drift and degradation as well as reducing power consumption.

2.2.2. Characteristics of thin-film transistors (TFT)

As an essential building block of active matrix-addressed flat-panel liquid crystal displays (AMLCDs), thin film transistors (TFTs) serve as a pixel switching device[22]. The pixels comprise liquid crystals of which the transmissive or reflective optical properties can be controlled by electrically charging or discharging them through TFTs[23]. In order to be used as a pixel TFT, there are some performance requirements that must be satisfied. For instance, low *leakage current* in the off-state is needed to avoid cross-talk and high *mobility* is required for high resolution and circuit speed. Typical *on/off ratios* should be in excess of 10^5 to properly charge and discharge the pixels[24].

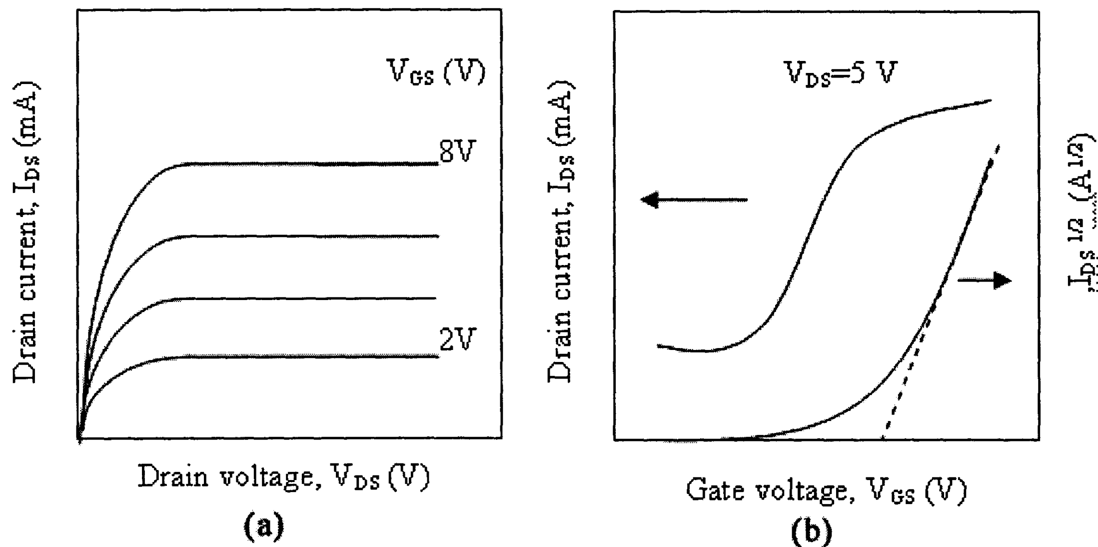

Figure 5. Characteristic curves of a thin film transistor. a) General output characteristics of TFT; (b) General form of transfer characteristics for V_{DS}=5 V. The graph shows extraction of threshold voltage V_{TH} by plotting $I_{DS}^{1/2}$ and V_{GS}.

As shown in Figure 5, output curve (a) and transfer curve (b) are generally employed to characterize thin-film transistors (TFT). Drain current (I_{DS}) is plotted against drain voltage (V_{DS}) for different values of gate bias (V_{GS}) in the output curve, which demonstrates the amplification nature of TFTs. Log drain current is plotted against gate voltage (V_{GS}) at a given drain voltage (V_{DS}) in the transfer curve. Various electrical parameters such as field effect mobility μ, threshold voltage V_{TH}, subthreshold swing and on/off ratio are extracted from these two curves. While the on/off ratio is easily obtained by reading the current level in the *on* and *off* state of the TFT in the output curve (see figure

5(a)), the threshold voltage (V_{TH}) is defined as the gate voltage at which the drain current dependence on the gate bias stops being exponential, more properly defined as the turn-on voltage.[25] The so called threshold voltage is extracted from a plot $I_{DS}^{1/2}$ and V_{GS}, according to the following equation.

$$I_{DS} = \frac{W}{2L}\mu C_i (V_{GS} - V_{TH})^2 \tag{2.10}$$

where I_{DS} is the drain current, W/L, the channel width to length ratio, μ, the carrier mobility, C_i, the gate oxide capacitance, V_{GS}, the gate voltage and V_{TH} the threshold voltage.

With knowledge of the geometry of the TFT structure and the gate oxide capacitance, the mobility μ of the TFT is generally obtained from the slope of transfer curve (see figure 5(b)) by utilizing the above equation.

In spite of differences in the operating characteristics, described below, most papers on TFTs adopt the conventional MOSFET modeling approach which is presented in this section.

2.2.3. Physics of thin film transistors

Figure 6 illustrates the structure of a conventional n-channel Metal Oxide Semiconductor Field Effect Transistor (MOSFET) and its energy band diagram when the MOSFET is turned on. As illustrated in figure 6 (a), the MOSFET consists of metal electrodes, gate oxide, sandwiched between gate electrode and semiconductor, and a single crystalline semiconductor which serves as a substrate at the same time. In contrast, thin film transistors (TFT) comprise active elements, i.e. metal electrodes, gate oxide and semiconductor, deposited on a separate substrate (see figure 6 (a) and 7 (a)). For TFTs, the semiconductor could either be polycrystalline or amorphous with a thickness less than a micron. As for MOSFETs, when a positive bias V_{GS} ($>V_{TH}$) is applied to the gate, a semiconducting n-channel is formed in the p-substrate by inverting the major charge carrier from holes to electrons, also called strong inversion, at the semiconductor/oxide interface (see figure 7(b)). Unlike conventional Metal Oxide Semiconductor Field Effect Transistors (MOSFET), organic (e.g. pentacene) and metal oxide (e.g. ZnO) TFTs operate in the accumulation regime, that is, by the accumulation of the major charge carrier, not in the inversion regime[26].

As illustrated in figure 7(b), when the gate is biased positively, electrons drawn toward the semiconductor/oxide interface fill the surface states and traps, creating trap charge Q_T[27]. Once available traps become filled, as the gate bias is further increased, the highly conducting n-channel will be created at the semiconductor/oxide interface, causing the bottom of conduction band (E_C) at the interface to be lowered relative to the Fermi level (E_F).

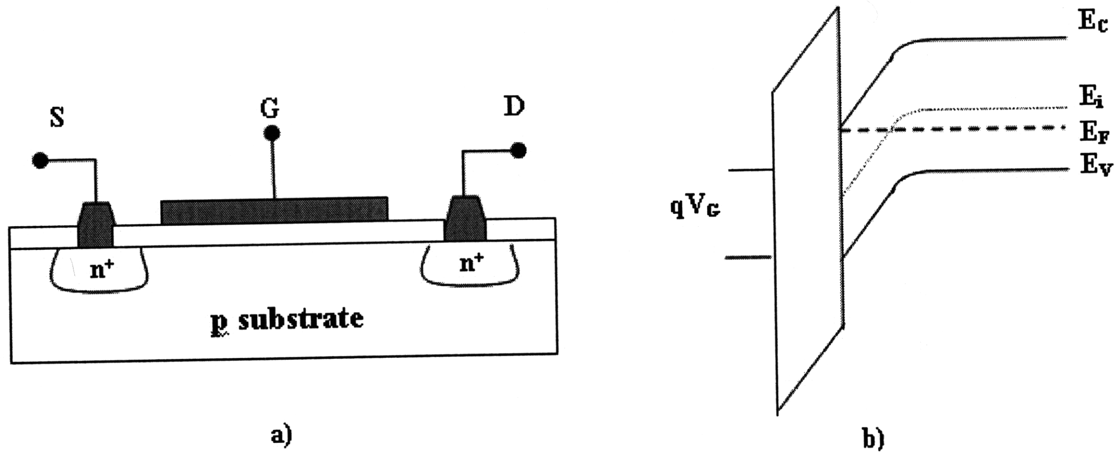

Figure 6. a) Cross-sections of a conventional n-channel MOSFET; b) Energy band diagram for an n-channel MOS under strong inversion, $V_{GS} > V_{TH}$. S: source electrode, G: gate electrode, D: drain electrode

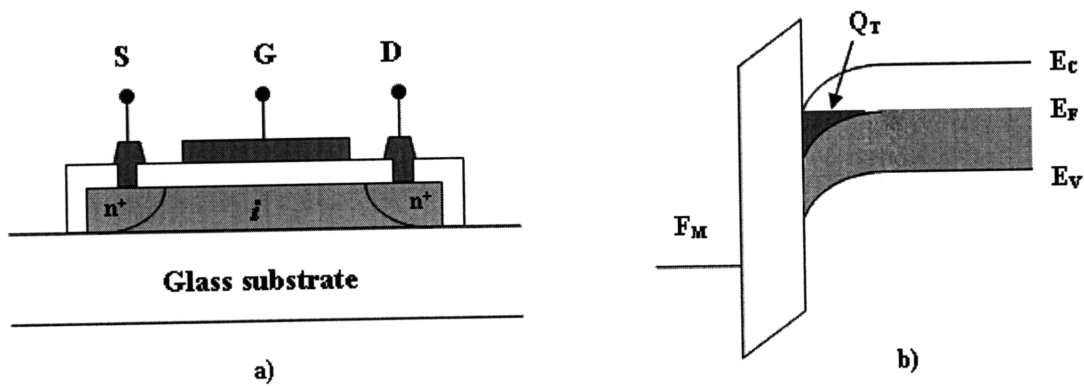

Figure 7. a) Cross- section of an n-channel thin-film field effect transistor; b) Energy band diagram for an n-channel TFT under large positive gate bias, resulting in formation of an electron channel[28]

Figure 8 represents the energy band diagrams of TFTs with film thickness $t_s < \lambda$ under (a) zero gate bias, (b) small positive gate bias and (c) turn-on voltage. Provided that the film thickness is thin enough ($t_s < \lambda$), the conducting n-channel is created through the film, resulting in carrier accumulation throughout.

(a) Zero gate bias

(b) Small positive gate bias

(c) Larger positive gate bias (under turn on voltage)

Figure 8. Energy band diagrams for MOS capacitors with a thin semiconducting layer, where $t_s < \lambda$.[28]

2.2.4. Volkenstein model

The Volkenstein model is presented here since it correlates chemisorptive capacity of a semiconductor and external influences such as an electric field and doping. Only the effect of an external electric field on the chemisorptive capacity will be dealt with here. For further discussion, it is essential to distinguish two distinct forms of chemisorption: the electrically neutral and charged forms. The electrically neutral chemisorption, more commonly called "weak" chemisorption, forms the bond between the gaseous molecules and the semiconductor without any localization of free electrons or holes in the crystal. However, these weakly chemisorbed particles acquire dipole moments while remaining electrically neutral. In contrast, charged chemisorption, i.e. strong chemisorption, involves the localization of a free carriers (electron or hole), contributing to charge on the surface.

The chemisorptive capacity, characterized by the total number of gaseous molecules adsorbed N, of a semiconductor consists of N^0 and $N\mp$, where N^0 and $N\mp$ correspond to the number of weakly chemisorbed particles per unit surface area and the number of charged particles chemisorbed per unit of surface, respectively. Here, the (-) sign

corresponds to acceptor-like or oxidizing gases (O_2, NO and NO_2) and the (+) sign represents donor or reducing particles. While the amount of the neutral form of chemisorption on the surface (N^0) is fixed by external conditions such as temperature T and pressure P, the position of the Fermi level (E_F) determines the number of charged species from chemisorption $N^{\mp}$. The chemisorptive capacity of a semiconductor N, composed of N^0 and $N^{\mp}$, is given by the equation (2.12) where $N^{\mp}$ is correlated to N^0 by equation (2.11). The meaning of the symbols used in equation (2.12) is clearly shown in figure 9(a) which illustrates the energy band diagram of a semiconductor where acceptor-like molecules (denoted as A) are adsorbed[29]. According to equation (2.12), the chemisorptive capacity of the surface is regulated by factors shifting the Fermi level E_F, in turn changing E_V^- or E_V^+, within the crystal, and by factors changing the degree of bending Vs of the bands[30].

$$N^{\mp} = N^0 \exp\left(\frac{E_a^{\mp} - E_s^{\mp}}{kT}\right) \qquad (2.11)$$

$$N = N^0 + N^{\mp} = N^0[1 + \exp\left(\frac{E_a^{\mp} - E_s^{\mp}}{kT}\right)] \quad where \quad E_s^{\mp} = E_v^{\mp} + V_s \qquad (2.12)$$

A: the local level of the chemisorbed particles (acceptor or donor)

E_S^- : the distance from the E_F to the bottom of the conduction band (E_C) at the semiconductor/gas interface

E_S^+: the distance from the E_F to the top of the valence band (E_V) at the semiconductor/gas surface.

E_A^- : the distance from the acceptor level (A) to the bottom of the conduction band at the semiconductor/gas interface

E_A^+ the distance from the acceptor level (A) to the top of the valence band at the semiconductor/gas interface

E_V^-: the distance between E_F and the bottom of the conduction band (E_C) in the bulk

E_V^+: the distance between Fermi level and the top of the valence band in the bulk

V_S: surface potential

$N_{VGS=0V}$: the adsorption capacity of semiconductor in the absence of a field

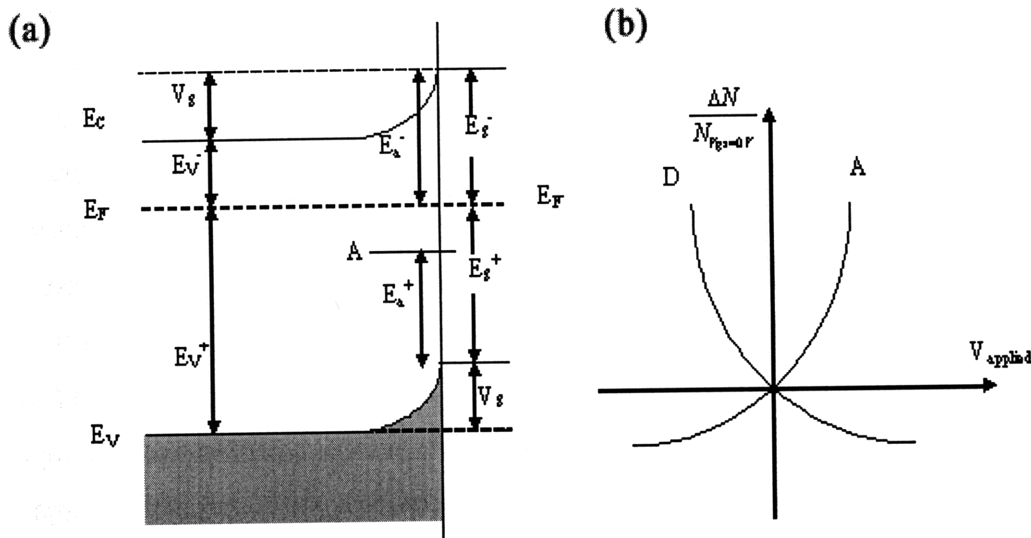

Figure 9. (a) Energy band diagram of a semiconductor with chemisorbed molecules (denoted A) on it. (b) Relative change in the adsorptive capacity $\frac{\Delta N}{N_{V_{GS}=0V}}$ of the surface of an n-type semiconductor as a function of applied bias via electrode.

In figure 9(b), a positive field, $V_{applied}$, makes the semiconductor negatively charged. As illustrated in Figure 9(b), the application of the field to the semiconductor results in additional adsorption or desorption depending on the polarity of the bias and the nature of the gases and semiconductor. For example, the application of positive bias on an n-type semiconductor causes additional adsorption of the acceptor-like gaseous molecules such as O_2 , NO or NO_2 while it result in the desorption of donor-like gaseous molecules such as H_2 and CO. Adsorption of oxidizing molecules shift the E_F at the surface of the crystal downward (increasing E_S^-), while adsorption of reducing particles shift it upward (decreasing E_S^-).

2.3. $InGaZnO_4$

2.3.1. Transparent ionic amorphous oxide semiconductors (IAOS)

Large-area electronics, mainly driven by the need for large-area displays, was created by the discovery of hydrogenated amorphous silicon (a-Si:H) by Spear and

Lecomber in 1975[30]. Owing to the capability of achieving large-area deposition at low temperature in thin film format, amorphous silicon (a-Si:H)) is now a fundamental building block of thin film transistors (TFT) used in active-matrix flat-panel displays despite its several demerits; low electron mobility ($1cm^2V^{-1}s^{-1}$), inefficient use of backlight due to its opaque nature and device degradation under visible light illumination. Therefore, tremendous efforts are being made to find transparent and amorphous semiconductors with relatively high electron mobility.

Another mainstream of research called 'transparent electronics' is rapidly growing for both military and consumer applications. Transparent conducting oxides (TCOs) such as indium tin oxide (ITO, Sn-doped In_2O_3), Al-doped ZnO, and Sb-doped SnO_2 have been intensively commercialized as transparent electrodes for flat panel display, organic light emitting diodes (OLEDs), and solar cells.[31] [32] However, their application has been limited to metals only, mainly due to the absence of p-type transparent semiconducting oxides. Ever since Kawazoe et al. demonstrated the possibility of making the p-type transparent oxide semiconductor $CuAlO_2$[33] in thin film format, both p-type and n-type transparent oxide semiconductors are vigorously investigated for future transparent electronics. Often, conventional amorphous materials with covalent bonding, e.g. glass, chalcogenide glasses and glassy oxide semiconductors, have very small carrier mobilities such as 10^{-4} $cm^2V^{-1}s^{-1}$. [34] As a logical step, amorphous oxide semiconductors with strong ionic bonding, i.e. ionic amorphous oxide semiconductors (IAOS), are explored as candidate materials for transparent electronics, especially to address their low electron mobility. Nomura et al. reported transparent and flexible thin film transistors deposited at room temperature from amorphous $InGaZnO_4$ (a-IGZO)[35] with high electron mobility ($>10cm^2V^{-1}s^{-1}$), which suggests possible solutions to the limitations that hydrogenated amorphous silicon (a-Si:H) have; low electron mobility(1 $cm^2V^{-1}s^{-1}$), rigid and fragile glass substrate. High electron mobility, unusual for the amorphous state, is achieved by employing heavy metal oxides, owing to spatial overlap between vacant s-orbitals of neighboring cations at the conduction band minimum. The electron transport mechanism of ionic amorphous oxide semiconductors (IAOS), which gives high electron mobility, will be explained later in this thesis.

Lastly, transparent IAOS have received much attention since their low temperature fabrication processes are more compatible with 'flexible electronics'. Flexible electronics, characterized by electronic circuits fabricated on organic substrates, for applications such as wearable electronics and paper displays, necessarily require low temperature processes ($<150^0C$) since polymer substrates can not withstand the high temperatures that current Si MOS technology employs.

2.3.2. Properties of amorphous $InGaZnO_4$

Formation of IAOS such as amorphous $InGaZnO_4$ requires an extremely high cooling rate, i.e., amorphous $InGaZnO_4$ (a-IGZO) can be fabricated only in the form of a thin film not in bulk form. Thin films of amorphous $InGaZnO_4$ (a-IGZO) are usually obtained from a polycrystalline ceramic target by using physical deposition techniques such as pulsed laser deposition and radio frequency sputtering at room temperature (RT)[36].

As a n-type semiconductor, amorphous $InGaZnO_4$ (a-IGZO) is transparent with an optical bandgap (E_g) of 3.1eV~3.3eV [40] for films with carrier concentrations of $\sim10^{13}cm^{-3}$ and $\sim10^{20}cm^{-3}$, respectively. It is known that the density of amorphous $InGaZnO_4$ (a-IGZO) is 5.9 gcm^{-3}.

Figure 10 (left) shows the phase diagram of thin films deposited at room temperature in the In_2O_3-Ga_2O_3-ZnO ternary system. As illustrated in Figure 10, the phase transforms from amorphous to polycrystalline only at high composition ratio of Zn or In. The amorphous structure of $InGaZnO_4$ thin films was confirmed by X-ray diffraction measurements as shown in Figure 11. Local density approximation (LDA) - relaxed structure of amorphous $InGaZnO_4$ (a-IGZO), constructed by ab initio calculations, is illustrated in Figure 12 along with that of single crystalline $InGaZnO_4$ (sc-IGZO) for comparison. Single crystals of $InGaZnO_4$ (IGZO) are composed of alternating stacks of InO_2^- and $(GaO/ZnO)^+$ layers. In^{3+} ions are located at octahedral sites, forming two dimensional edge-sharing networks of InO_6 octahedra. Ga^{3+} and Zn^{2+} ions randomly occupy trigonal-bipiramidal sites and are coordinated by five oxygen ions. For a-IGZO, edge-sharing networks of InO_6 only partially remain and the coordination number of each cation is reduced from that of sc-IGZO. As illustrated in the right diagram of figure 12, InO_6 and

GaO_6 coexist with less numbers of InO_5 and GaO_5 pentahedra, leading to a decrease in the density of a-IGZO by 5% compared to that of crystalline IGZO.

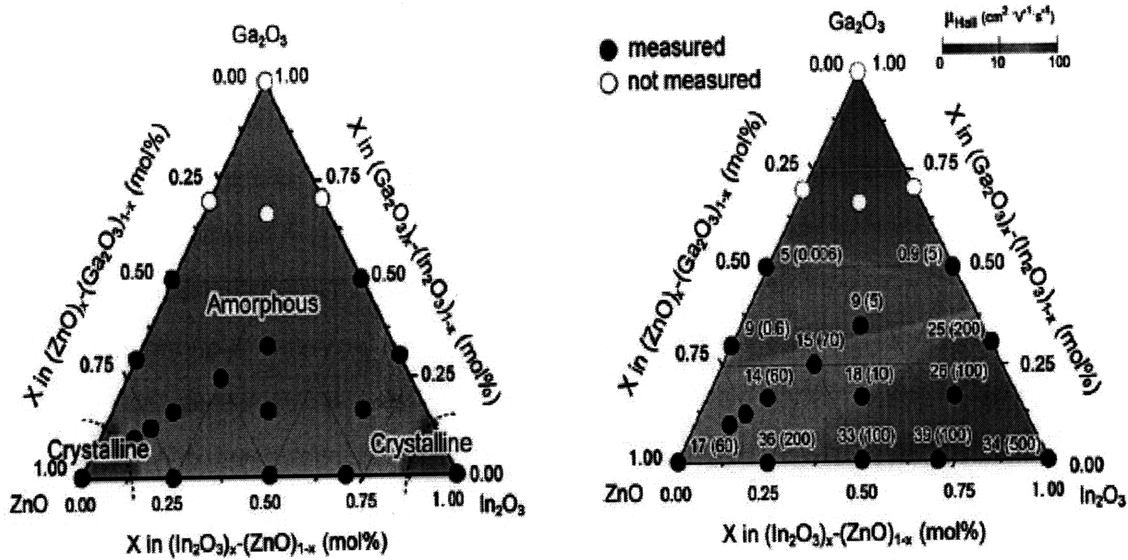

Figure 10. The amorphous formation region in the In_2O_3-Ga_2O_3-ZnO system (left) and the electron mobilities and carrier concentrations (right) evaluated from the Hall effect for amorphous thin films in the In_2O_3-Ga_2O_3-ZnO system [38]. The thin films were deposited on a glass substrate by pulsed laser deposition under the atmosphere of Po_2=1Pa. Numbers in parenthesis denote carrier electron concentration ($x10^{18}cm^{-3}$)

Right diagram in Figure 10 shows electron mobilities and concentrations evaluated from the Hall effect for amorphous thin film. Electron mobilities range from 5 to 39 $cm^2v^{-1}s^{-1}$. While the highest value of mobility, 39 $cm_2v^{-1}s^{-1}$, obtained around the samples containing the maximum In_2O_3 fraction; the lowest value of the mobility is obtained in Ga-rich samples. However, Ga^{3+} is known to play a role as carrier killers and to stabilize the a-IGZO film[37]. It is reported that as-deposited Ga-free films undergo fast resistivity change just after the deposition[41].

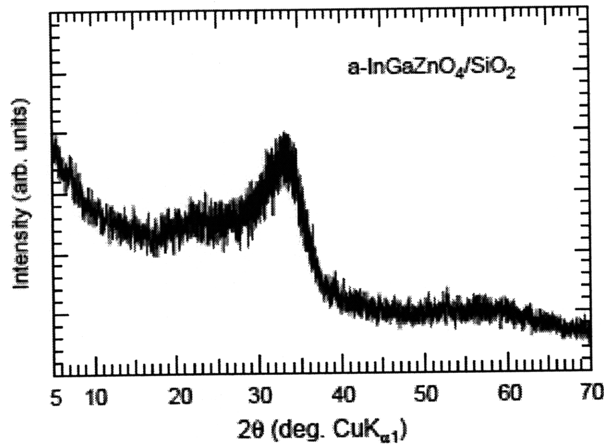

Figure 11. XRD pattern of a-IGZO film deposited on SiO_2 glass substrate by PLD[38]

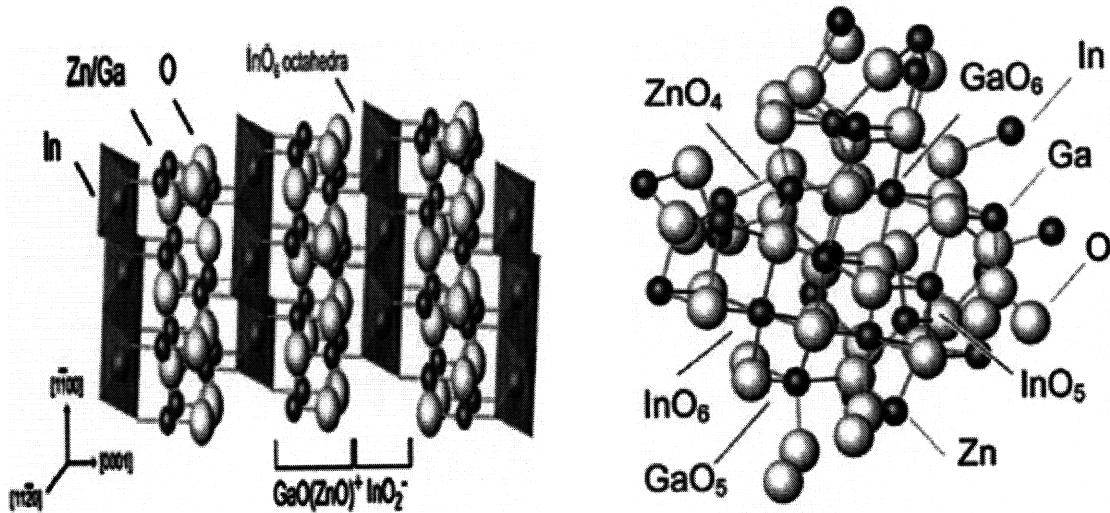

Figure 12. Structure of single crystalline $IGZO_4$. (left) LDA-relaxed structure of amorphous $IGZO_4$ containing $(InGaZnO_4)_{12}$ atoms. (right) MO_n (M=metal cation, n=integer) indicates a specific coordination structure with MO_n polyhedra[39].

2.3.3. Electron transport of ionic amorphous oxide semiconductor

Generally, it is believed that amorphous semiconductors exhibit much deteriorated electron mobilities than associated crystalline counterparts as known for hydrogenated amorphous silicon (a-Si:H). This is because tail states and subgap density of states, originated from structural disorder and defects, hinder electron transport[40]. For example, the electron mobility of hydrogenated amorphous silicon (a-Si:H) is 1 $cm^2V^{-1}s^{-1}$ which is significantly lower than that of single crystalline silicon, However, ionic oxide

semiconductors have large electron mobilities over 10 $cm^2V^{-1}s^{-1}$ even in the amorphous state, which are almost comparable to those in crystalline oxide semiconductors. These unique electron transport properties can be understood from the electronic structure of ionic oxide semiconductors.

The electronic structures of ionic oxides are vastly different from those of covalent semiconductors as illustrated in Figure 13. In case of covalent semiconductors, for instance Si, both conduction band minimum (CBM) and valence band maximum (VBM) are made of hybridized sp^3 orbitals. In contrast, CBMs and VBMs of ionic oxide semiconductors are primarily composed of vacant s-orbitals of metal cations and oxygen 2p-orbitals, respectively. Owing to extended spatial spread of the vacant s-orbital, direct overlap between the s-orbitals of the neighboring cations is possible in heavy metal oxides, and therefore the effective mass of electrons is small in these oxides. Nevertheless, this alone cannot explain why high electron mobility is maintained only in ionic oxide semiconductors even in the amorphous structure. Whereas sp3 or p-orbitals with strong spatial directivity can be easily disrupted by structural randomness, spherical s-orbitals are not largely altered by disordered local structures. Therefore, for covalent semiconductor, disorder caused by amorphous structure forms rather deep and high-density localized states below CBM and above VBM, causing carrier trapping and eventually leading to the degradation of mobility.

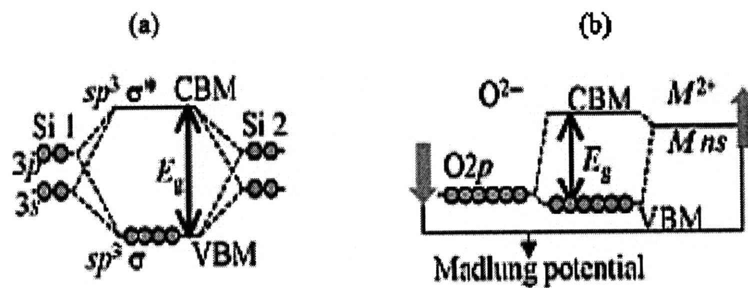

Figure 13. Comparison of energy bandgap formation between (a) covalent semiconductor and (c) ionic semiconductor ($M^{2+}O^{2-}$)[41]

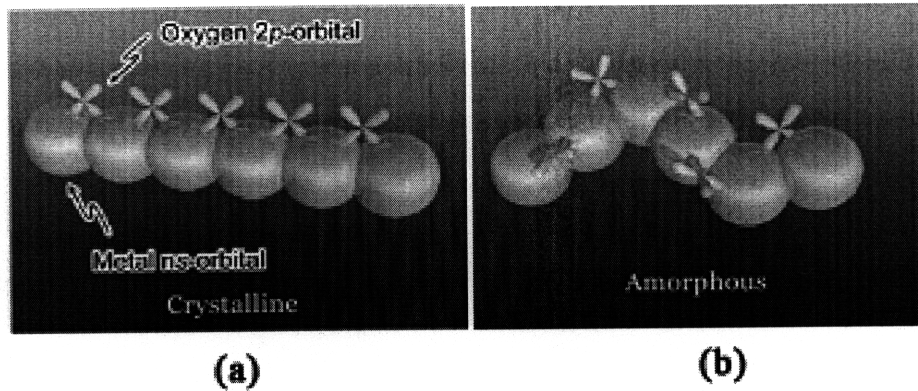

(a) **(b)**

Figure 14. Schematic illustration of orbitals in (a) crystalline and (b) amorphous structures of ionic oxide semiconductors.[42] This image is valid for oxides of heavy metal cations with $(n-1)d^{10}ns^{0}$ $(n \geq 5)$ configuration.

However, CBMs of ionic oxide semiconductors, made of s-orbitals, are not significantly changed by local disorder due to their spherical shape and the electron mobility is not significantly affected [45] as shown in figure 14. Furthermore, in order for ionic amorphous oxide semiconductors to have large electron mobilities comparable to those of the corresponding crystals, the constituing metal cations should have an electronic configuration $(n-1)d^{10}ns^{0}$ $(n \geq 5)$, i.e. heavy post transition metal cations. For amorphous $InGaZnO_4$ (a-IGZO), In^{3+} ions $(4d^{10}\ 5s^{0})$ well satisfy this criterion and contribute to the enhanced electron mobility ($\geq$ 10 $cm^2V^{-1}s^{-1}$). This is why the highest mobility of thin film a-IGZO is achieved around the maximum compositional ratio of In_2O_3.

3. Experimental procedure

3.1.Model system

A schematic of the IGZO TFT array deposited on a p-type silicon substrate is illustrated in figure 15. Each gray area (see figure 15(a)) represents an IGZO TFT and the numbers denote the channel lengths and widths of the IGZO TFTs. A photograph of the sample inside the test chamber is shown in figure 15(b). Cross sectional and top schematic views of each IGZO TFT are given in figure 16. Buried-gate type amorphous $InGaZnO_4$ (a-IGZO) channel thin-film transistors (TFTs) (figure 16) were employed to investigate gas adsorption on the a-IGZO semiconducting channel. A heavily p-doped (boron) silicon wafer serves both as the gate electrode and substrate. Amorphous $InGaZnO_4$ (a-IGZO), is sputter deposited on top of thermally grown 100 nm thick SiO_2 gate insulator. The a-IGZO film, a semiconducting metal oxide (SMO), is 70nm thick; thin enough to ensure that the applied gate bias influences band bending in the a-IGZO at the gas/solid interface and in turn chemisorption at this interface. Lastly, Pt / Ti bilayers were used as source and drain where the Ti layers serve to promote adhesion of the Pt layer to the SiO_2 gate oxide. Table 1 lists the key components of the IGZO TFT and their roles.

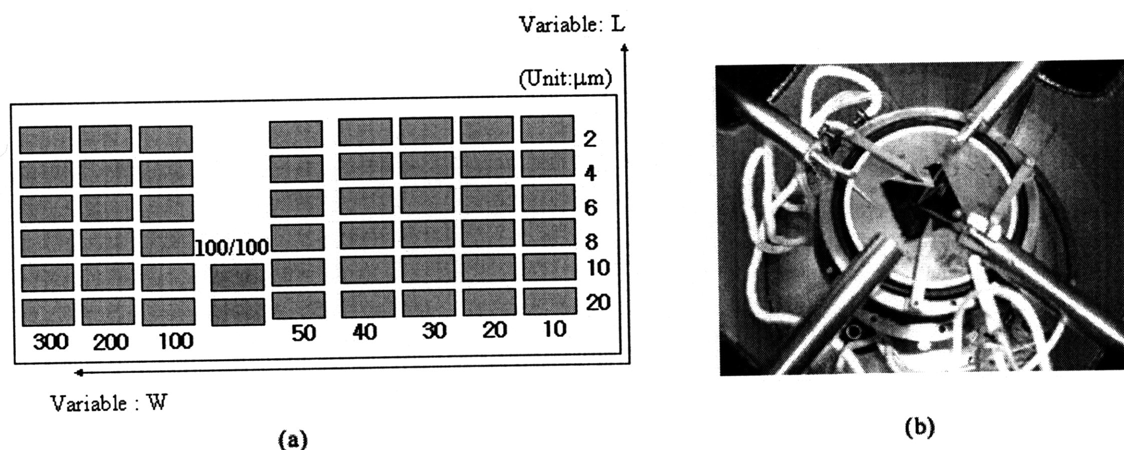

Figure 15. (a) Schematic of IGZO TFTs deposited onto a heavily doped p-type silicon substrate. (b) The top view image of TFTs placed inside a custom-designed microprobe station. Numbers in (a) denotes the channel lengths and widths of the TFTs.

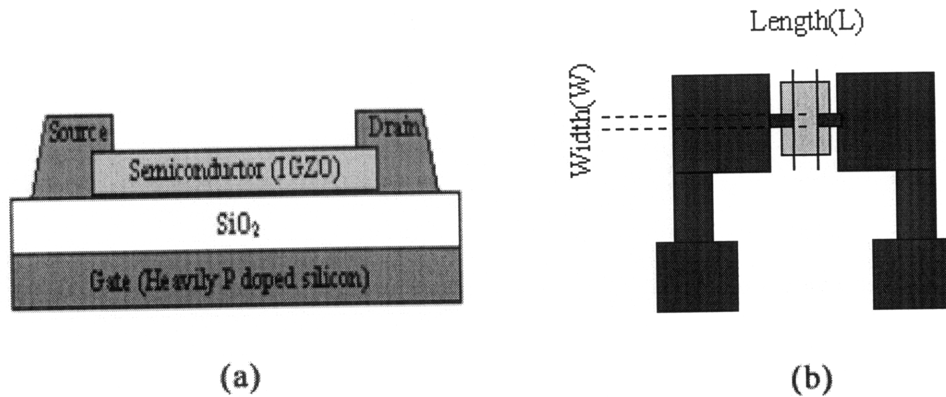

Figure 16. (a) Schematic of cross-sectional view of the a-IGZO TFT structure. (b) Top view of IGZO TFT

The amorphous nature of $InGaZnO_4$ offers several potential advantages over polycrystalline semiconductor metal oxides. Low temperature processing of the sensing materials makes them more readily compatible with CMOS technology, leading, in turn, to miniaturization and cost reduction. Furthermore, complications of electron conduction, involved with grain boundaries in polycrystalline semiconducting metal oxides, are avoided. High electron mobilities, reported for a-IGZO, ensure high channel conductance, desirable for improvement of sensitivity.

Table.1. Key components of the IGZO TFT

Element	Role
Amorphous $InGaZnO_4$ (70nm)	Gas sensing layer (Semiconducting layer)
SiO_2 (100nm)	Gate insulator
Heavily p-doped silicon	Gate electrode and Substrate
Pt/Ti	Source/Drain electrodes

3.2.Electrical measurements for gas sensor performance

Figure 17 shows the gas sensor measurement setup and a photograph of the custom-designed test chamber. Mass flow controllers (MFC), MKS 647A, were utilized to regulate the flow rate and concentrations of gases under investigation. Gases are mixed in a mixing chamber before they are introduced to the test chamber for sensor measurement. Table 2 lists the test gases, their roles and concentrations used in this thesis research. The gas flow rate was kept constant at 1000 sccm for all measurements in order to exclude any problems involved with flow rate change, gas consumption by the sensor and adsorption and desorption at the walls of the pipelines and test chamber. A relatively high flow rate, 1000 sccm, was employed due to the large test chamber volume; at least 10 to 15 minutes were required to replace the atmosphere of the test chamber at a flow rate of 1000 sccm. The concentrations of test gases are controlled according to equation (3.1)

$$Desired\ C\ of\ component\ gas\ A = C\ of\ component\ gas\ A \times \frac{F(component\ gas\ A)}{F(Total)} \quad (3.1)$$

where C and F denote concentration and flow rate, respectively.

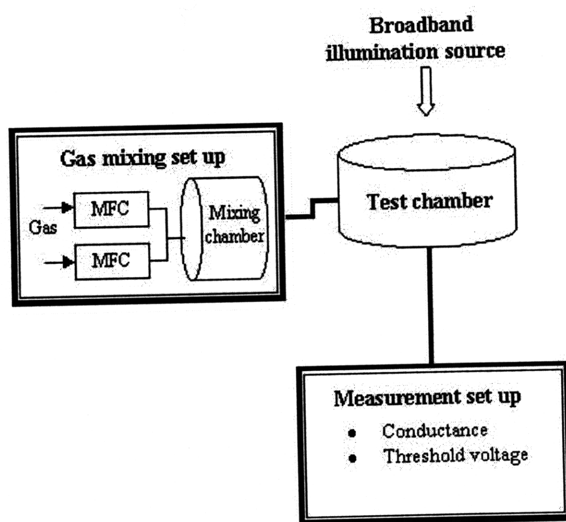

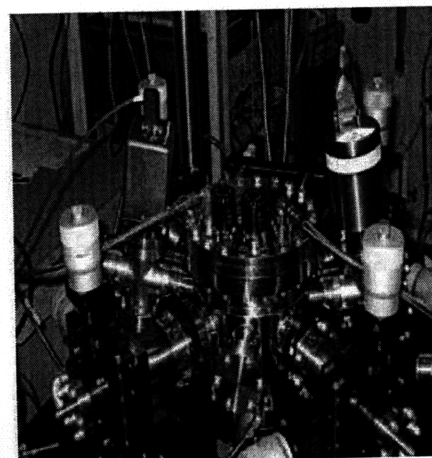

(a) (b)

Figure 17.(a) A schematic of gas sensor measurement set-up (b) A photograph of the custom-designed microprobe station

As shown in figure 17(b), the custom-designed microprobe station, equipped with four micromanipulators and a 2" heater capable of reaching 1200^0 C, is used for electrical measurements (see figure 15(b)). This probe station can be enclosed, allowing for measurements in vacuum or controlled environments. Also, an optical microscope is placed above the microprobe station, not shown here, enabling the observation of micron size features. In this study, an optical microscope was utilized to provide broadband illumination as well as serving to align the microprobes with the TFT electrodes.. The light was magnified ~ 12 times with the aid of built-in lenses. However, because the intensity of light was significantly attenuated in passing through the window in the vacuum chamber of the microprobe station, an additional calibration step is needed to determine the light intensity. This calibration step is planned for the future.

For all measurements, an HP4142B Modular DC source/monitor was utilized and controlled with appropriate home-made labview software. DC current-voltage measurements (section 4.1 and 4.2) were performed to measure the sensor performance and photoresponse of IGZO TFTs. For these two studies, IGZO TFTs, with zero gate voltage, were used instead of IGZO TFRs to reduce measurement noise. , Labview software was programmed to allow continuous monitoring of the IGZO channel conductance while gate biases were applied in order to investigate the influence of the field effect on chemisorption at IGZO surfaces. Lastly, transistor characterization was performed with an HP4142B Modular DC source/monitor and the effective threshold voltage[1] was calculated from a V_{GS} versus $I_{DS}^{1/2}$ plot (see section 2.2.2)

Table 2. Test gases for electrical measurements

Gas	Concentration	Role
Air, N_2		Carrier/
O_2	100%	Oxidizing
NO_2	10 ppm in air	Oxidizing
NO	50 ppm a100ppm in N_2	Oxidizing

4. Results

[1] In this context, the turn-on voltage or threshold voltage is defined as the voltage necessary to drive the device into accumulation.

4.1.Sensor performance at reduced temperature

The gas sensor performance of $IGZO_4$ thin film was examined at different temperatures using DC conductance measurements. Figure 18 shows conductance change of IGZO thin film sensors when exposed to 10ppm NO_2 in synthetic air (50% R.H., 25°C) at different temperatures; room temperature, 60°C and 100°C. IGZO thin film show typical n-type semiconductor behavior; the conductance decreases when exposed to oxidizing gases (NO, NO_2 and O_2), and increases when exposed to reducing gases(H_2, CO and NH_3). This thesis will limit investigation of sensor response only to oxidizing gases. The sensitivity, defined as $\frac{R_{NO_2} - R_{Air}}{R_{Air}}$, to 10ppm NO_2 as a function of operation temperature is shown in Figure 19. Note that the sensitivity of IGZO thin film to NO_2 gas at room temperature is significantly high (87) and decrease as operation temperature increases.

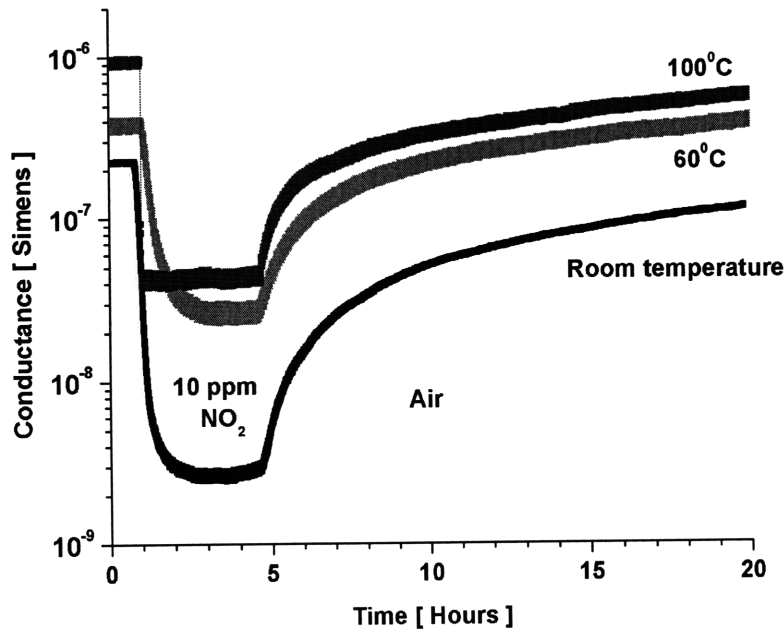

Figure 18. Sensor response of IGZO films to 10ppm NO_2 in synthetic air (50% R.H., 25°C at different temperatures; room temperature, 60°C and 100°C.

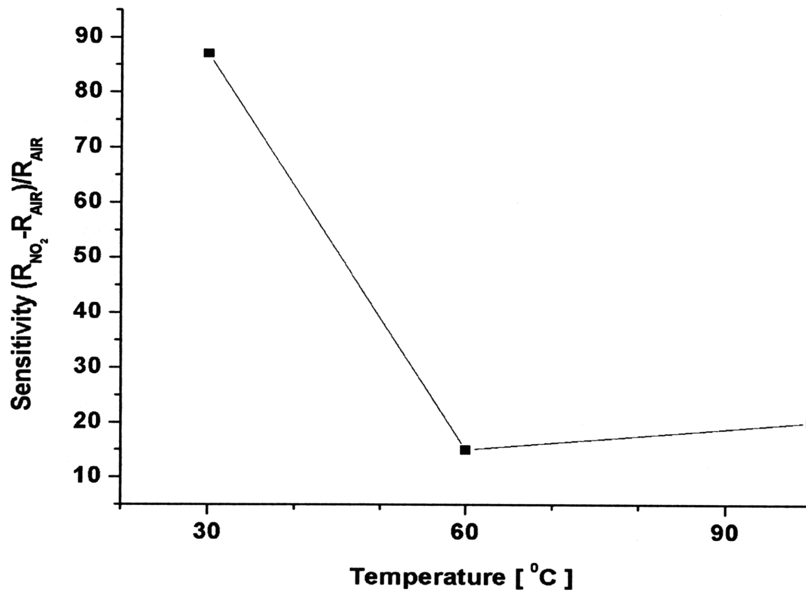

Figure 19. Temperature dependent sensitivity of IGZO thin film to 10ppm NO_2 in synthetic air (50% R.H., 25°C)

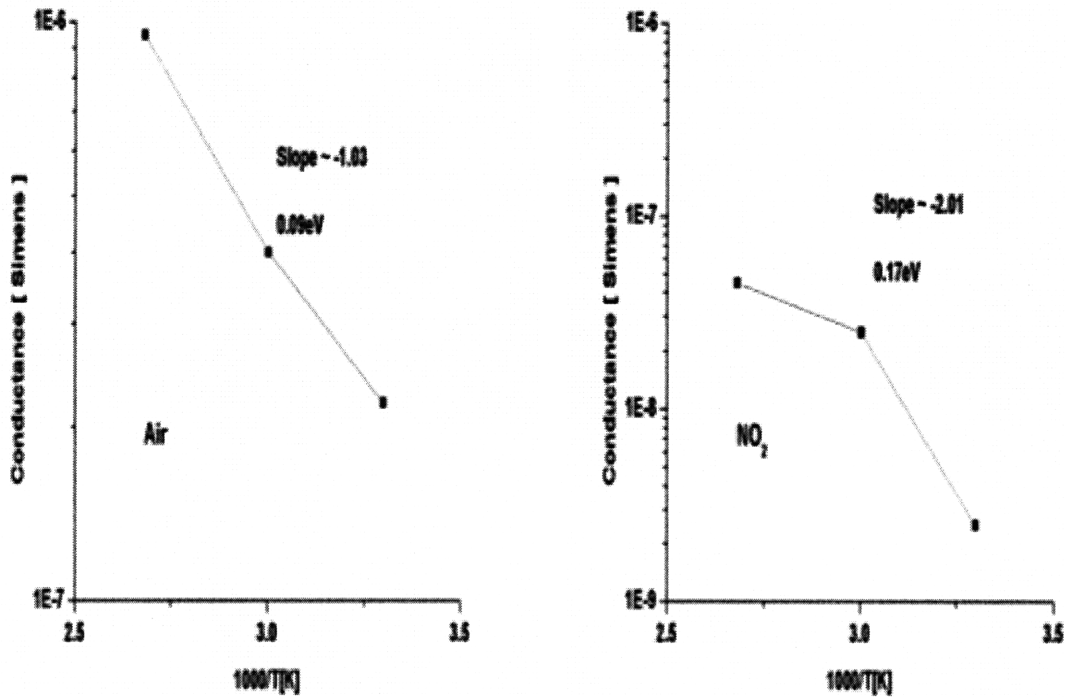

Figure 20. Temperature dependence of conductance (a) under synthetic air (b) under 10ppm NO_2 in synthetic air

This result, the temperature dependence of the sensitivity, can be understood by typical temperature dependence of carrier concentration of semiconductor; increase in

carrier concentration as temperature increases due to thermal carrier generation. Figure 20 demonstrates temperature dependence of carrier concentration, reflected as conductance, which gives additional information on activation energies of oxygen and NO_2. From the slope of Figure 20, the activation energies of oxygen and NO_2 are extracted as 0.09eV and 0.17eV respectively. Compare to that of ZnO thin film (~ 1eV[16] for O_2), activation energies of IGZO is significantly small. This well explains the fact that IGZO thin film show significantly higher sensitivity to NO_2 at relatively reduced temperature.

Summary of key observations

1. The IGZO thin film show typical n-type semiconductor behavior; the conductance decreases when exposed to oxidizing gases (NO, NO_2 and O_2), and increases when exposed to reducing gases(H_2, CO and NH_3)
2. The sensitivity of IGZO thin film to NO_2 gas at room temperature is significantly high (87) and decrease as operation temperature increases.
3. The extracted activation energies of oxygen and NO_2 are significantly lower that that of polycrystalline ZnO.

4.2.Conductance measurement under illumination

To examine the effect of light on desorption and re-adsorption kinetics of a-IGZO thin film resistors (TFRs), particulary at reduced temperatures, the channel conductance of a TFT was measured when the IGZO was exposed to broadband illumination under controlled chemical analytes and temperatures. Photo-induced desorption of oxygen and NO_2 from a-IGZO was examined as shown in figure 21 and figure 22, respectively.

Initially, samples were placed into the measurement chamber and vacuum annealed under high vacuum (2~5x 10^{-6} Torr) for an hour. The samples were then heated to 300^0C and held there for an hour to accelerate the desorption of pre-chemisorbed gaseous molecules. To control the amount of chemisorbed gaseous molecules adsorbed onto the IGZO thin film, 100% oxygen was introduced into the chamber while holding the temperature at 300^0C. Then, the IGZO TFRs were annealed at 300^0C for an hour. Finally,

the IGZO TFRs were cooled to room temperature over 3hours. The procedure for obtaining a reproducible reference state is summarized in the table below.

Table 3. Annealing procedure followed prior to sensor characterization

	Details
1.	high vacuum (2~5x 10^{-6} Torr) anneal for an hour
2.	Heat to 300^{0}C
3.	Hold at 300^{0}C for an hour under high vacuum
4.	Anneal at 300^{0}C for an hour under 100% oxygen
5.	Cool to room temperature under 100% oxygen

The above annealing procedure resulted in a reproducible initial conductance level (4~5 x 10^{-7} S). However, these pre-treatments induced a breakdown of the gate dielectric of the IGZO-based thin film transistors after repetitive treatments.

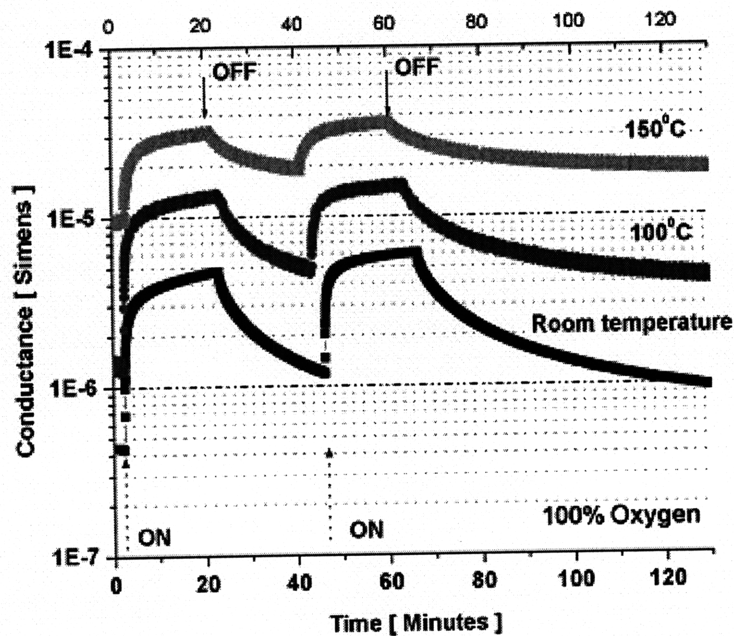

Figure 21. The channel conductance of a a-IGZO$_4$ thin film operating in a 100% oxygen atmosphere. The broad band light source is turned on and off according to the above figure.

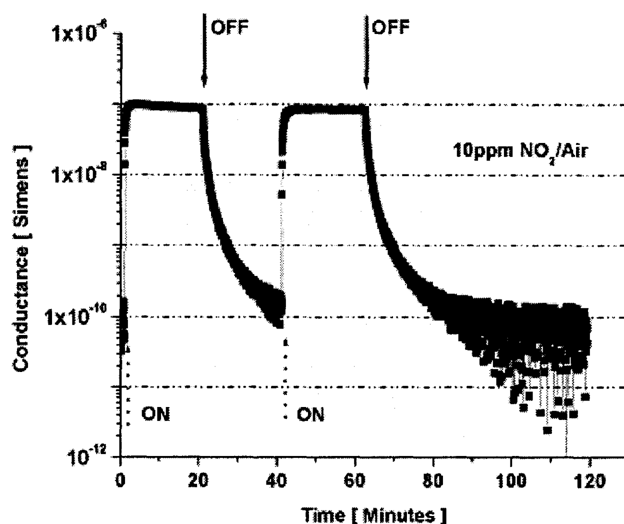

Figure 22. The channel conductance under the influence of 10 ppm NO_2/Air measured at room temperature. The broad band light source is turned on and off according to the above figure.

Photo-induced desorption of oxygen was investigated at three different operating temperatures; room temperature, 100^{0}C and 150^{0}C while the specimens were maintained under 100% oxygen (figure 21). Once the reference state was achieved by following the previously described procedure, the device was heated to the desired operating temperature. Then, a-IGZO TFTs were illuminated for 20 minutes, followed by removal of the light source for 20 minutes. The light was reapplied for 20 minutes and then turned off for more than an hour. The channel conductance is observed to instantaneously increases upon broadband illumination (see figure 23), followed by a gradual increase over time presumably due to desorption of electron trapping O_2 molecules. When the light source is removed, the channel conductance falls as shown in figure 21. The rapid decrease in channel conductance is presumably due to the combined result of loss of photoconductance, characterized by a more rapid drop in conductance on the time scale of the figure, and a more gradual drop due to the increased chemisorption of the electron trapping O_2 molecules.

The following rate equations are employed to fit the data and extract time constants of chemisorption on a-IGZO films.

$$G = G_0 + \Delta G \exp(-t/\tau) \quad for \quad adsorption \tag{4.1}$$

$$G = G_0 + \Delta G (1 - \exp(-t/\tau)) \quad for \quad desorption \tag{4.2}$$

where G is the film conductance at some time t , G_0 is the initial film conductance prior to illumination, ΔG is the conductance change from the maximum value of the channel conductance to the initial film conductance and τ is the characteristic time constant.

Table 4 summarizes the extracted time constants for desorption and re-adsorption of oxygen on IGZO film at temperatures of 30^{0}C, 100^{0}C and 150^{0}C.

Table 4. Time constants for oxygen desorption and re-adsorption on IGZO film

	Desorption	Re-adsorption
30^{0}C	19.6 min	35.3 min
100^{0}C	14.0 min	69.0 min
150^{0}C	13.1 min	117.7 min

The time constant for desorption of oxygen from the a-IGZO film, extracted from the first set of photo-induced desorption steps, decreases as the operating temperature increases, but weakly. This means that the desorption kinetics of oxygen are enhanced as the operating temperature increases. One observes the opposite for the oxygen re-adsorption kinetics. The time constant for re-adsorption of oxygen on a-IGZO film increases as the temperature increases, meaning that adsorption is apparently hindered by thermal energy when the operating temperature is above 100^{0}C.

For investigating the photo-induced NO_2 desorption from a-IGZO films, 10 ppm NO_2 in synthetic air was introduced into the measurement chamber, after the reference state was obtained, to allow for chemisorption of NO_2 on a-IGZO TFTs surface prior to the illumination studies. As shown in Figure 22, the channel conductance shows similar

response to the ones obtained for oxygen; conductance increases upon illumination and decreases upon removal of the light source. The time constants for re-adsorption and desorption of NO_2 molecules on the IGZO film, extracted by applications of equations (4.1) and (4.2) to the data, are summarized in Table 5. The chemisorption kinetics, both desorption and re-adsorption, of NO_2 molecules on IGZO film is very rapid compared to that of oxygen molecules (see table 4 and table 5).

Table 5. Time constants for NO_2 desorption and re-adsorption on IGZO film at room temperature

	Desorption	Re-adsorption
30^0C	0.68 min	2.6 min

Summary of key observations

1. Channel conductance (G) increases as operating temperature increases.
2. Rapid increase in channel conductance (G) is followed by gradual increase in channel conductance when the device is illuminated under the influence of 100% oxygen or 10 ppm NO_2/Air.
3. Rapid decrease in channel conductance (G) is followed by a gradual decrease, to the original value of the channel conductance, once the light source is removed under the influence of 100% oxygen or 10ppm NO_2/Air.
4. Time constants for photo-induced oxygen desorption from IGZO films show temperature dependant behavior; photo-induced desorption kinetics are enhanced as the operation temperature increases.
5. Time constants for re-adsorption of oxygen on IGZO film increase as the operation temperature increases; re-adsorption of oxygen molecules on IGZO film is hampered by thermal energy above 100^0C.
6. Re-adsorption and desorption kinetics of NO_2 molecules are much faster than that of oxygen molecules.

4.3. Field effect in $IGZO_4$ thin film transistors

4.3.1. Threshold voltage measurements

In an attempt to investigate the feasibility of using gate bias as a mean for reducing gas sensor operating temperatures, the threshold voltage, V_{TH}[2], was measured immediately following removal of the gate bias which had been maintained previously for a fixed period of time.

The gate bias effect on chemisorption of oxidizing species on IGZO was investigated by exposing an IGZO TFT to 100 ppm NO in N_2 gas at room temperature and examining the effect of gate bias on the threshold voltage, V_{TH}. First, the IGZO TFT was exposed to 100 ppm NO in N_2 gas for several hours prior to the application of a bias. Then, as illustrated in figure 23(b), gate voltages are applied as follows; successively higher negative gate biases, -10V, -20V and -30V, were each applied for 20 minutes, 0V for 3 hours, followed by successively higher positive gate biases, 20V, 30V and 40V each for an hour. V_{TH} measurements were performed at the end of the application of each gate voltage. As illustrated in Figure 23(a), V_{TH} decreased stepwise from 12.5 V to 6V after successively higher negative gate biases were applied and partially recovered after applying 0 volts for 3 hours. On the other hand, V_{TH} increased stepwise from 9V to 15V with successively higher positive gate biases. Considering the meaning of V_{TH}, a decrease in V_{TH} indicates an increase of carrier concentration in the channel and vice versa. This result can be attributed to gate voltage induced desorption and chemisorption for negative and positive gate biases, respectively, in compliance with respective decrease and increase in the Fermi energy in the IGZO film. It is known that the desorption of NO is sluggish at room temperature, this result strongly suggests that gate bias can indeed serve as a powerful tool for desorbing NO, even at room temperature.

[2] In this context, the turn-on voltage or threshold voltage is defined as the voltage necessary to drive the device into accumulation

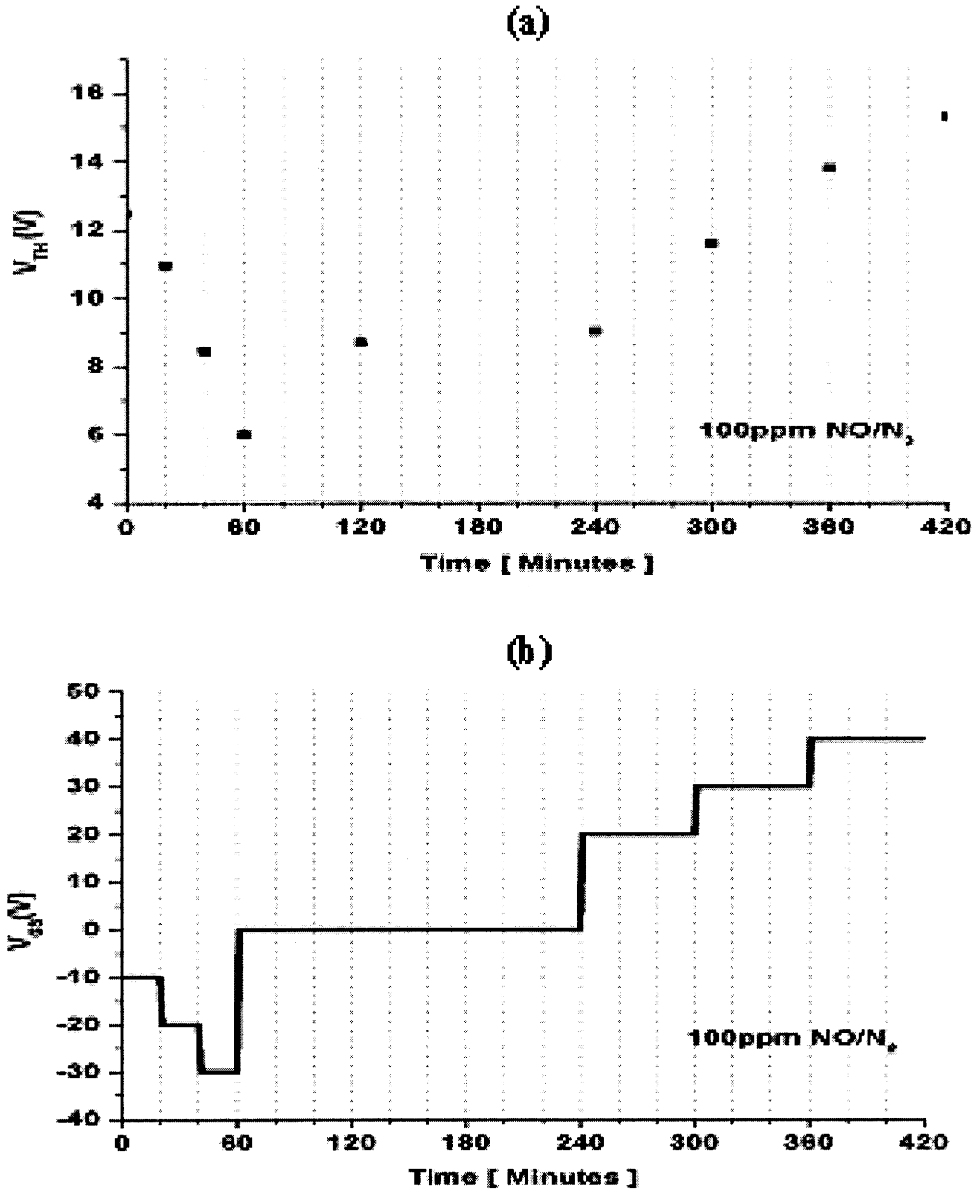

Figure 23. The effect of gate bias on (a) threshold voltage V_{TH} of a $IGZO_4$ TFT exposed to 100 ppm NO in N_2 (b) Applied gate bias V_{GS} as a function of time

Summary of key observations

1. The threshold voltage, V_{TH},decreases after successive application of negative gate biases, indicative of desorption of NO at room temperature.
2. The threshold voltage, V_{TH}, partially recovers after applying zero gate bias for 3 hours, showing that field-induced desorption is reversible at room temperature.
3. The threshold voltage, V_{TH} , increases after successive application of positive gate biases, indicative of chemisorption of NO at room temperature.

4.3.2. Transient conductance of $IGZO_4$ TFT under applied gate bias

Conductance changes were examined under constant gate bias following a change in gas environment; high vacuum (2~5 x10^{-6} Torr), 100% oxygen, 50ppm NO in N_2 following initial pretreatments described as in Table 1 above.

The gate biases are applied as illustrated in figure 24(b) and 25(b) under the influence of 100% oxygen and high vacuum, respectively; successively higher magnitude negative biases are applied, alternating with 0 V, starting from -5V to -30V, with a period of 10 minutes. Then, the same gate voltage application scheme is employed for positive gate biases. The corresponding change in conductance upon gate bias application is recorded as shown in figure 24(a) and 25(a). The channel conductance decreases and increases instantaneously upon negative and positive gate bias application, respectively in compliance with decrease and increase of the Fermi level of the IGZO film, followed by the gradual increase and decrease in conductance during application of negative and positive gate voltages. As an indicator of the carrier concentration in the IGZO film, the channel conductance at 0V is recorded after either negative or positive gate bias application. As shown in figure 24, the conductance at 0 V increases after successive application of negative gate biases, implying field-induced desorption of chemisorbed molecules. This conductance change is larger under the presence of oxygen molecules than that under high vacuum. On the other hand, under the influence of 50 ppm NO/N_2, a slightly different scheme of gate biases are applied as shown in figure 26(b). The magnitude of negative or positive biases, $\pm 5V, \cdot \pm 10V \cdot and \pm 15V$, are applied over successively increasing time alternating with 0 V. This is done because of the detection limits of our instruments, i.e. the a-IGZO films become too resistive to measure accurate changes in conductance when gate biases below -15V are applied.

Summary of key observations

1. The conductance decreases instantaneously upon negative gate bias application. This is true for all environments: 100% oxygen, high vacuum, 50 ppm NO/N_2.

   $V_{gs}^0 < 0V \rightarrow G\downarrow$ (the superscript 0 denotes the time at 0)

2. The conductance ($G_{V_{gs<0V}}$) gradually increases over time by a significant amount while the gate bias is maintained at negative gate bias. This is true for all environments: 100% oxygen, high vacuum, 50 ppm NO/N_2

   $Vgs^t<0V \rightarrow G\uparrow$ (t denotes the change in time)
3. The conductance increase instantaneously upon positive gate bias applications. This is true for all environments: 100% oxygen, high vacuum, 50 ppm NO/N_2.

   $V_{gs}^0>0V \rightarrow G\uparrow$
4. The conductance ($G_{V_{gs>0V}}$) gradually decreases over time by a relatively smaller amount while the gate bias is maintained at positive bias. This is true for all environments: 100% oxygen, high vacuum, 50 ppm NO/N_2.

   $Vgs^t>0V \rightarrow G\downarrow$
5. After negative gate bias application, the conductance measured at zero gate bias ($G_{V_{gs=0V}}$) increases by two orders of magnitude, from $6x\ 10^{-8}$ to $6x10^{-6}$ S under the influence of 100% oxygen
6. After positive gate bias application, the conductance measured at zero gate bias ($Gv_{gs=0V}$) decreases by one order of magnitude from $6x10^{-5}$ to $5x10^{-7}$ S under the influence of 100% oxygen.
7. After negative gate bias application, the conductance measured at zero gate bias ($G_{V_{gs=0V}}$) increases five fold, from $2x\ 10^{-6}$ to $1x10^{-5}$ S under high vacuum.
8. After positive gate bias application, the conductance measured at zero gate bias ($Gv_{gs=0V}$) decreases nearly 5 fold, from $1x10^{-5}$ to $3x10^{-6}$S under high vacuum.

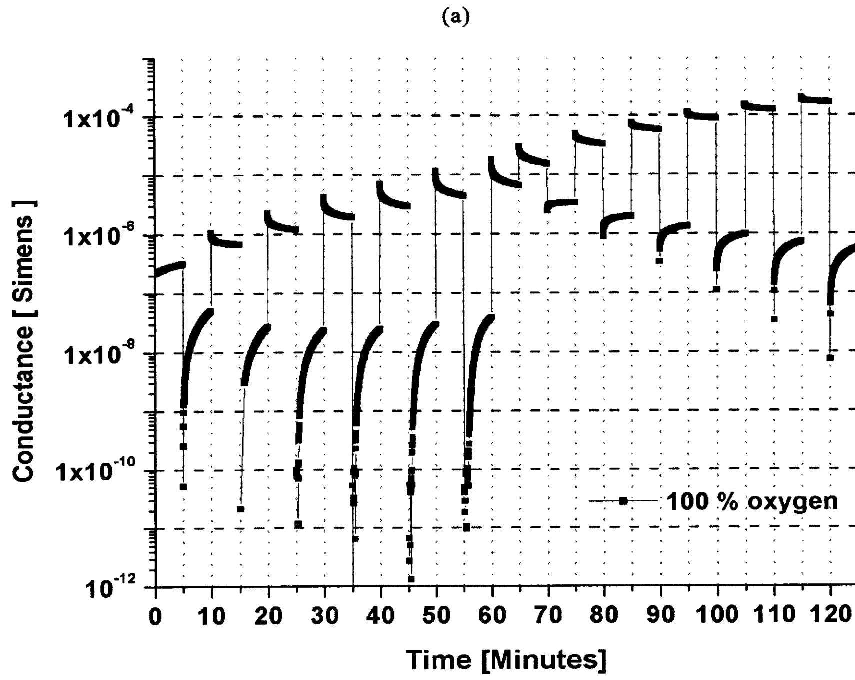

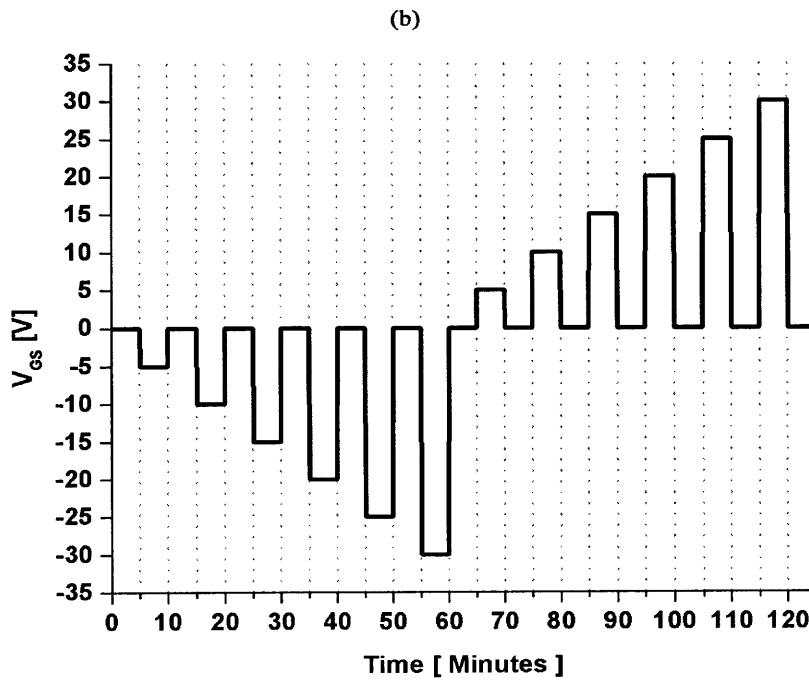

Figure 24. (a) Conductance changes of a-IGZO thin film under the influence of 100% oxygen upon gate bias application (b) Applied gate bias versus time. Successively higher magnitude negative or positive biases are applied alternating with 0 V.

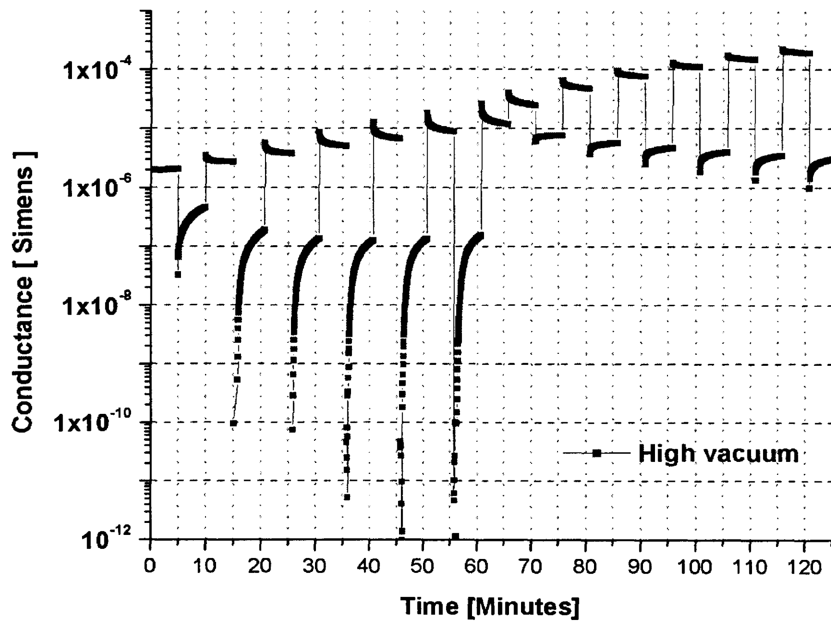

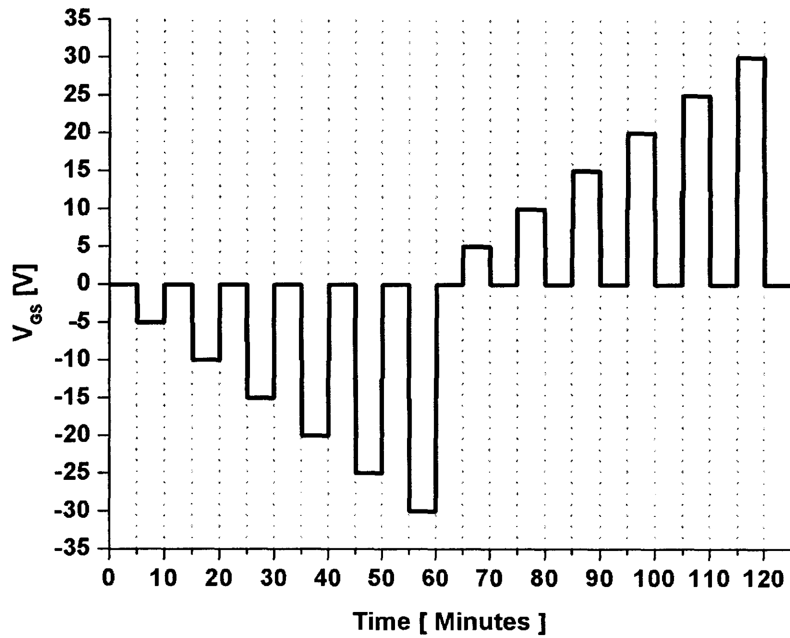

Figure 25. (a) Conductance changes of a-IGZO thin film under high vacuum upon gate bias application (b) Applied gate bias versus time. Successively higher magnitude negative or positive biases are applied alternating with 0 V.

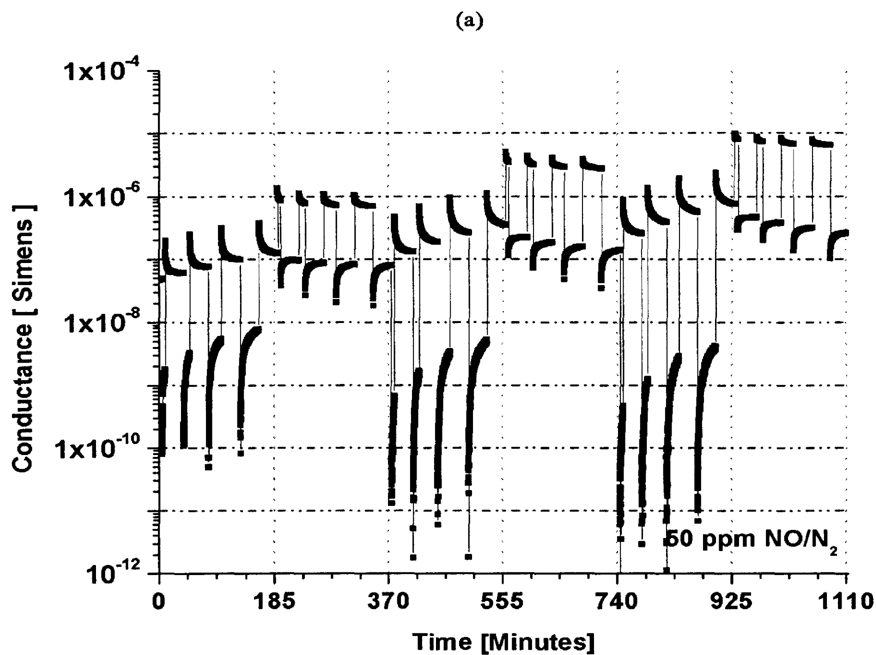

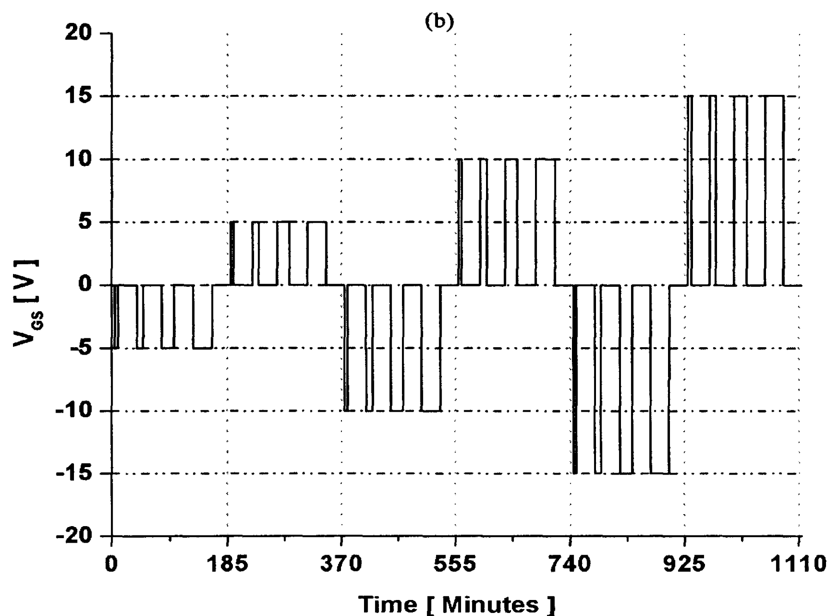

Figure 26. (a) Conductance changes of a-IGZO thin film under 50 ppm NO/N_2 upon gate bias application (b) Applied gate bias versus time. Negative or positive biases, $\pm 5V, \pm 10V \cdot and \pm 15V$, are applied over successively increasing times alternating with 0 V

4.3.3. Transient conductance under negative bias at different temperature

In order to confirm that previously observed conductance changes result from chemisorption induced by the field effect, additional experiments were required. Provided that chemisorption is a thermally activated process, conductance changes should exhibit temperature-dependent behavior if they are indeed chemisorptive processes. For the purpose of investigating the effect of gate bias on chemisorption in depth, transient channel conductance measurements were performed over extended times of more than 5 hours, as shown in Figure 27. Channel conductances were recorded while a gate bias of -10V was held for 5 hours at various temperatures; room temperature (RT), 100°C and 150°C.

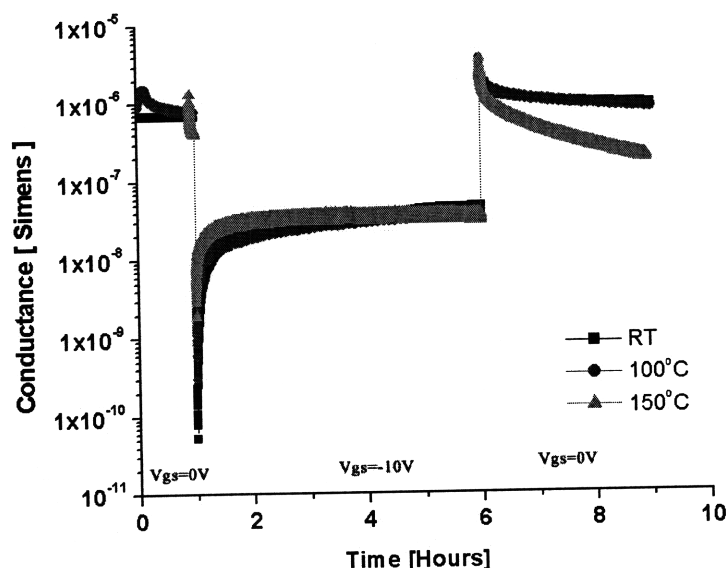

Figure 27. Conductance upon negative gate bias (V_{GS}) applications under a 50 ppm NO in N_2 atmosphere as a function of temperature. V_{GS}= -10V is applied for 5 hours at different temperatures; Room temperature, 100°C, 150°C. V_{GS} = 0V is held prior to and following negative gate bias applications.

Prior to measurement, as described earlier, the pre-treatment schedule summarized in Table 3 was performed on samples to exclude any unknown effects by pre-adsorbed gaseous molecules. The devices were then exposed to 50 ppm NO/N_2 balance without any gate bias applied. Then, 10V of gate bias was applied to the device for 5 hours and the corresponding transient conductance recorded. Afterwards, a zero gate bias was applied for

3 hours to allow re-adsorption of NO molecules. After this field-induced desorption study at room temperature, TFTs were heated to 100^0C and held there for sufficient time to stabilize before any additional studies were initiated. The same sequence of gate biases, 0V for an hour, -10V for 5 hours and 0V for 3 hour, were applied to the TFTs and the transient conductance measured. The same courses of measurements as at 100^0C were repeated at 150^0C.

As illustrated in figure 27, charge carrier depletion, characterized by a rapid decrease in conductance, is followed by the field-induced electron de-trapping, exhibited by the gradual increase in conductance, when a negative gate bias is applied. By employing equation (4.2), $G = G_0 + \Delta G(1-\exp(-t/\tau))$ *for desorption*, time constants for field-induced desorption were obtained as a function of temperature (see Table 4). As shown Table 6, desorption kinetics are improved as the operation temperature increases, indicating that the observed transient conductance, induced by the field effect, is indeed involved with the chemisorptive processes.

Table 6. Time constants for field-induced desorption at various temperatures

	Time constants [Hour]
Room temperature	1.88
100^0C	1.64
150^0C	0.5

Summary of key observations

1. The conductance decreases instantaneously upon negative gate bias application (-10V) under the influence of 50 ppm NO/N_2 for investigated temperatures; room temperature, 100^0C and 150^0C

   V_{gs}^0<0V→ G↓ (0 denotes that time=0)

2. The initial conductance drop (right at the negative gate bias application) is the largest at room temperature and decreases as temperature increases; the initial conductance level at elevated temperature is high due to thermal carriers and saturates to a relatively similar value.

3. The conductance ($G_{V_{gs}<0V}$) gradually increases by large amount, i.e. from 4.5 $\times 10^{-11}$ to 5×10^{-8} S, at room temperature while the gate bias is maintained at V_{GS}= -10V. A gradual increase in channel conductance, under the application of negative gate bias, occurs for all investigated temperatures.
4. The conductance changes show temperature-dependent behavior upon negative gate bias application under the 50 ppm NO/N_2 environment; the higher the operating temperature, the faster the field-induced desorption of NO.
5. The conductance changes show temperature-dependent behavior after the removal of the negative gate bias, i.e. 0V; the higher the temperature, the faster the re-adsorption of NO resulted from the field effect.

4.4. Conductance measurement under both illumination and field effect

Based on the results described so far, the application of illumination and the field effect can aid the chemisorption process, i.e. desorption and re-adsorption of gas molecules on IGZO film at much reduced temperatures. In an attempt to verify that light and the field effect can serve together as a means of reducing the operating temperature of semiconducting metal oxide (SMO) sensors, the following experiment was devised.

Initial conditions were controlled by the procedures described in the previous section 4.3.3. Gate biases were applied as shown in figure 28(b) under a 50 ppm NO/N_2 gas atmosphere; +5V and -5V are applied between the gate and source, alternating with 0V each for 5 minutes, starting with zero gate bias, i.e. V_{GS} = 0V. After the first cycle of gate bias application, corresponding to 25 minutes, the light is turned on and the same sequence of gate biases is applied once again. This is followed by application of -10V and -15V of gate bias alternating with 0V for 5 minutes. The shaded area in figure 28(a), after 25 minutes, indicates when the TFTs are under broadband illumination. Under dark condition, V_{GS} = -5V results in the field-induced desorption of NO molecules, represented as the shaded circle in the left of figure 28(a), occurring from 15 to 20 min. Once illumination is begun, the channel conductance increases due to the combined effect of photoconductance and photo-induced desorption of NO molecules (indicated as the arrow on the top of the figure 28 (a)). Under illumination, V_{GS} = -5V is not low enough to induce similar

conductance changes to the one previously observed without illumination. A corresponding gate bias of approximately V_{GS} = -10V is required to cause a similar gate bias induced desorption as observed in the shaded circle on the right of figure 28(a). Thus a stronger field effect is needed to obtain similar level of desorption since chemisorbed gases are already partially desorbed with the aid of light.

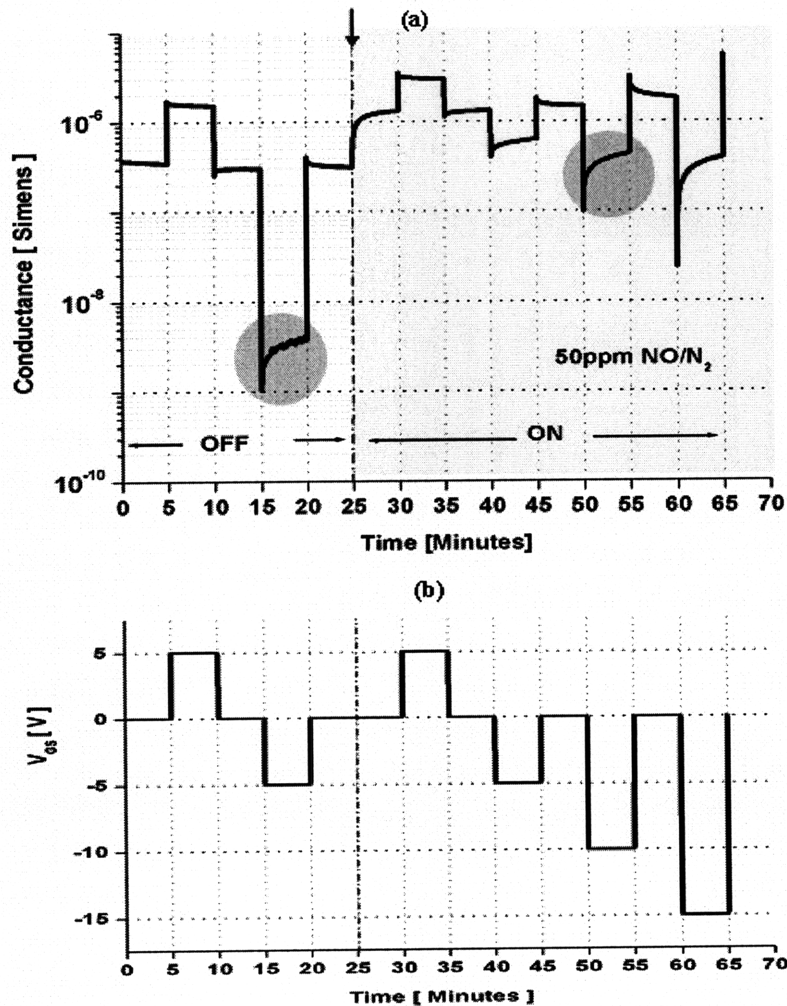

Figure 28. Channel conductance of IGZO TFT when the gate bias and broad band illumination are applied under 50 ppm NO/N_2 environments (a). Applied gate bias vs time (b). Illumination started at 25 min, indicated by the arrow at top of figure.

Summary of key observations

1. Under dark condition, -5V resulted in field-induced desorption of NO molecules at room temperature, reflected as a channel conductance change from 1×10^{-9} to 4×10^{-9} S over 5 minutes.
2. The channel conductance increases upon illumination at room temperature due to photo-induced desorption of NO molecules.
3. Under illumination, the -5V induced channel conductance change is only from 4×10^{-7} to 5×10^{-7} S over 5 minutes, indicating a smaller level of desorption of NO molecules compared to that without illumination. .
4. Under illumination, -10V caused a channel conductance change from $1\text{X}10^{-7}$ to 4×10^{-7} S, indicating comparable field-induced desorption to that of -5V without illumination.

5. Discussion

5.1.Enhanced chemisorption kinetics of amorphous IGZO

It is generally believed that charge transfer, associated with chemisorption, is an extremely slow process. For instance, E.Comini reported that SnO_2 exhibited a response time of several hours and an effectively infinite recovery time for NO_2 at room temperature. Therefore, most studies on gas sensors are usually performed at high temperature (>300^{0}C) to enhance kinetics.

As a relatively new material, little research has been done on amorphous IGZO as a gas sensor material; only Kang et. al.[12] suggested amorphous IGZO as a possible oxygen sensor material at low temperature given its strong response to oxygen partial pressure variation at or near ambient temperature. Before discussing the adsorption kinetics of amorphous IGZO, it is worthwhile introducing the charge transfer model in greater detail.

In the investigation of oxygen chemisorption on single crystal ZnO, Gatos et. al. defined the effective adsorption energy E_a as the thermal activation barrier for charge transfer associated with the chemisorption process. The charge transfer rate at the semiconductor-gas interface R_{ct} is given by the following equation[13].

$$R_{ct} = A_n v_T n_b \exp\left(\frac{qV_s}{kT}\right) N_p(P) \exp\left(-\frac{E_a}{kT}\right) - rate\ of\ thermal\ desorption$$

(5.1)

where each term is defined as follows.

V_s : the potential barrier height (band bending) at the SMO surface

A_n: Capture cross section for electrons

V_T: Thermal velocity of conducting electrons

N_b; The bulk density of free electrons

N_p: The density of physisorbed(unoccupied) species (states)

Np is a function of pressure P

q: absolute value of electronic charge

E_a: Effective adsorption energy (thermal activation energy)

The first term in equation (5.1), $A_n v_T n_b \exp\left(\frac{qV_s}{kT}\right) N_p(P) \exp\left(-\frac{E_a}{kT}\right)$, represents the charge transfer process due to chemisorption at the semiconductor/gas surface. It can be thought of as that chemisorption that occurs when electrons with energy sufficient to penetrate the surface barrier height V_s, characterized by $n_b \exp\left(\frac{qV_s}{kT}\right)$, are captured by activated states. These activated states, characterized by $N_p(P)\exp\left(-\frac{E_a}{kT}\right)$ are generated when physisorbed molecules are excited into metastable states in which they can capture electrons from the semiconductor. The thermal desorption rate, the second term in equation (5.1), should be subtracted since the thermally desorbing gases, donating electrons to the surface, decrease the number of physisorbed states, in turn reducing the activated states. If the operating temperature is low enough to neglect the thermal desorption rate, the rate limiting factors in the chemisorption process are the surface energy barrier V_s and the thermal activation E_a for bulk electrons and gases molecules, respectively. The activation energy is a significant rate-limiting factor to chemisorption occurring at room temperature. For instance, when Ea, determined for oxygen adsorption on single crystalline ZnO[13], is 0.72 eV, the exponential term, exp (-0.72eV/kT), reduces the rate of charge transfer by a factor of 10^{-13}. To summarize, electrons must penetrate the surface barrier V_s in order to be captured at the surface and gaseous species must overcome the energy barrier E_a for chemisorption to occur. These two rate limiting factors, especially E_a, are responsible for the extremely slow chemisorption process at room temperature.

However, as shown in figure 18, the adsorption kinetics of NO_2 on amorphous IGZO thin film is extremely fast even at room temperature. Considering that almost 10 minutes is required to replace the atmosphere of the test chamber, the amorphous IGZO responds to NO_2 within a few minutes even at room temperature. The somewhat slow response to NO_2 at 60^0C might be due to previously chemisorbed NO_2 from the first exposure at room temperature. This also can be confirmed by the fact the sensor responds to the NO_2 almost instantaneously at 100^0C.

In order to determine the activation energy of the amorphous IGZO film, equation (5.2) is employed. By fitting the conductivities of IGZO film under air and 10 ppm NO_2 to equation (5.2) as a function of temperature, the activation energy E_a can be extracted from the slope of the Arrhenius plot (see figure 18).

$$\sigma(T) = \sigma_a e^{-E_a/kT} \tag{5.2}$$

As shown in figure 20, the activation energies for O_2 and NO_2 under dark condition are obtained as 0.09eV and 0.17eV, respectively, which is markedly lower than that of polycrystalline ZnO (1eV). This small thermal activation energy for IGZO thin film could be the source of the fast NO_2 adsorption kinetics observed for this particular material at much reduced temperatures.

Another reason for the fast adsorption kinetics of IGZO could stem from its amorphous nature. Generally, band tails in amorphous materials, originated from structural disorder and defects, extend into the band gap, thus possibly offering more surface sites for gaseous molecules to chemisorb.

Also, a relatively small activation energy for conductance of indium oxide in thin film form (0.037eV)[53] is reported under dark conditions. Interestingly, E.Comimi et al. also reported that indium oxide showed a response time of 10 min under 3 ppm NO_2, indicating significantly rapid adsorption kinetics. Given that the electronic structure of IGZO is mainly dominated by s-orbitals of In_2O_3 (see section 2.3.3), the In_2O_3 might be responsible for fast kinetics observed for IGZO.

5.2.The influence of illumination on chemisorption at semiconductor/gas interfaces

To date there have been only few publications relating to the effect of light on the sensing properties of Metal Oxide Gas Sensors (MOGSs).[43,44,45,46] These studies investigated the utility of illumination as a potential tool for enhancing sensitivity and kinetics of MOGSs and demonstrated increased sensitivity and reversible response of SnO_2 and In_2O_3 sensors to CO and NO_2 at ambient temperature. This is in contrast to the response of non-illuminated samples which was negligible and very sluggish. These results suggest that photo-activation could replace thermally activated adsorption/desorption processes on the semiconductors surface.

In this thesis, photoconductivity measurements were performed to examine photo-activated chemisorption and kinetics of an IGZO film under the influence of 100% oxygen and 10 ppm NO_2/Air. As shown in figure 21 and 22 (see section 4.2), the IGZO film exhibited similar conductance change to the illumination cycle under both 100% oxygen and 10 ppm NO_2/Air environments: a rapid increase in channel conductance (G) is followed by a gradual increase in channel conductance upon irradiation and rapid decrease in channel conductance (G) is followed by a gradual decrease once the light source is removed. This observed conductance change is attributed to photon-induced desorption , also called photodesorption, schematically illustrated in figure 29.

In the dark, in case of an n-type semiconductor shown in figure 29(a), the surface states, located in the band gap, accept electrons from the conduction band and are partially filled. As a result, a positive space charge layer, i.e. depletion layer, is formed, giving rise to upward band bending at the semiconductor/gas interface. Upon band-gap irradiation, electron-hole pairs are created via interband generation and those within the space charge layer are driven apart by the existing space charge field[47]: Electrons are driven into the bulk while holes are driven towards the surface (see figure 30(b)). Then, photodesorption takes place by recombination of photogenerated holes with electrons trapped by the chemisorbed species. As a consequence, the adsorbed species change from a chemisorbed to a physisorbed state which can then thermally desorb at relatively low temperatures.

Provided that the time scale of desorption[48] of molecular and atomic oxygen vary in an extremely wide range from 10^{-13} to 10^{5} s, an initial rapid increase in channel conductance is attributed to the photogeneration of electron-hole pairs, whereas the photon-induced surface desorption[49] is responsible for the subsequent gradual increase in channel conductance.

Upon cessation of irradiation, the fast recombination of photogenerated electron-hole pairs occurs, on the time scale of 10^{-12} s, giving rise to the rapid decrease in channel conductance. Then, remaining electrons diffuse back to the semiconductor surface, inducing re-adsorption of gaseous molecules. This accounts for a gradual change in channel conductance. To sum up, fast initial rise and fall in the channel conductance, each corresponds to the generation and recombination of electron-hole pairs, followed by slow

rise and decay in the conductance associated with photodesorption and readsorption of gaseous molecules, respectively.

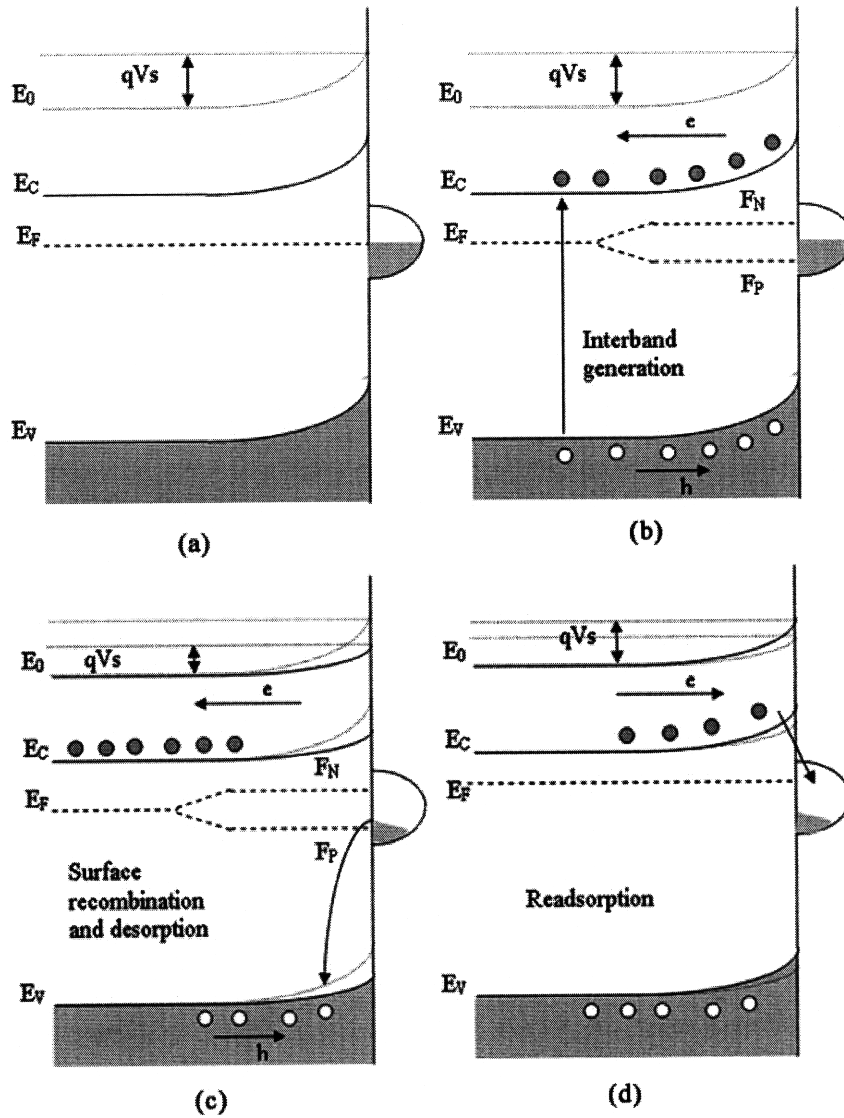

Figure 29. Energy band diagram of photon-induced desorption upon band-gap irradiation for an n-type semiconductor. Gray area represents states or band populated with electrons.

As shown in figure 22 (section 4.2), the photodesorption of oxygen from IGZO films was examined at temperatures of 30°C, 100°C and 150°C. First of all, the magnitude of the photoresponse, i.e. the increase in conductance upon illumination, is the largest at room temperature and decreases as operating temperature increases. This result is

consistent with the photoresponse study by Zhang[50,51] on a polycrystalline ZnO film in which the photoresponse decreases as the temperature increases above 300 K. This may be due to chemisorbed oxygen molecules being desorbed at the higher temperatures even before irradiation, leaving relatively small amounts of chemisorbed oxygen molecules to be desorbed by photo-activation.

In terms of the oxygen desorption kinetics, Zhang[49] reported significant enhancement for polycrystalline ZnO film as the operating temperature increases. On the contrary, there is only a small increase in photodesorption kinetics in the case of amorphous IGZO films: i.e. the time constants for photo-induced oxygen desorption decrease as the operating temperature increases, but weakly, as summarized in Table 3. This small increase in oxygen desorption kinetics can be partially ascribed to the amorphous nature of IGZO film. Whereas photodesorption of polycrystalline semiconductors can occur, not only at the semiconductor/gas interface, but also at grain boundaries, photo-induced desorption take place only at free surfaces in the case of amorphous semiconductors. Time constants for re-adsorption of oxygen on IGZO films increase as the operation temperature increases. Unlike photodesorption kinetics, re-adsorption of oxygen molecules on IGZO films is hampered by thermal energy above 100^{0}C. (see Table 3). This result agrees well with the previous observation, i.e. the sensitivity decreases as operating temperature increases from room temperature to 100^{0}C. This indicates that thermally-activated desorption of oxygen molecules is a dominant process at semiconductor/gas interface above 100^{0}C. Lastly, it should be noted that there is an increase in the dark conductivity which is maintained following irradiation, indicating the permanent photodesorption of oxygen from the IGZO film.

In this thesis, time constants of the photodesorption and readsorption processes are obtained by by fitting to simple exponential functions given below characterized by single time constants for each process. However, different time constants may be involved in the photodesorption and readsorption processes.

$$G = G_0 + \Delta G \exp(-t/\tau) \quad \textit{for} \quad \textit{adsorption} \tag{4.1}$$

$$G = G_0 + \Delta G (1 - \exp(-t/\tau)) \quad \textit{for} \quad \textit{desorption} \tag{4.2}$$

Electrons thermally freed from traps during photodesorption may be retrapped once or many times before recombination with photogenerated holes; a possible source of multiple time constants. A variety of possible recombination centers, such as oxygen vacancies and surface states, with different recombination cross-sections and velocities would make the recombination process even more complicated[50].

Re-adsorption and desorption of NO_2 molecules, as shown in figure 23, are much faster than that of oxygen molecules. Irradiation produces a steep rise to a relatively constant channel conductance followed by a fast, then slower decay (when the light is turned off) corresponding to the two mechanisms suggested above. A strikingly small time constant (0.68 min) might indicate that NO_2 photodesorption is extremely fast for this particular semiconductor, IGZO. However, there is alternative explanation for this observed behavior. Taking into consideration that the slow rise in the photoconductance is associated with photodesorption, the contribution of NO_2 photodesorption to the photoresponse is much reduced compared to that of oxygen (see figure 23). One of possible reasons could be that the illumination intensity utilized during this study is only enough to induce small amounts of photodesorption of chemisorbed NO_2 molecules, noticed as steep rise in conductance, since NO_2 is a strong oxidizing gas.

On the other hand, the decay of photoconductance, due to readsorption of NO_2, exhibits similar but a faster decrease in conductance compared to that of oxygen, which is consistent with results obtained in section 4.1. : The IGZO film responds to NO_2 at room temperature within a few minutes.

A study on the photocurrent of ultrafine In_2O_3[52] particle layers reported that the photocurrent decay time of ultrafine In_2O_3 particle layers under air is given as 2.7 min at room temperature. The In_2O_3 might play a role in fast decay with unknown reason.

5.3.The influence of the field effect on chemisorption at semiconductorgas interfaces

As reported in section 4.3.2, conductance changes examined under constant gate bias exhibit similar behavior under the influence of high vacuum (2~5 x10^{-6} Torr), 100% oxygen, and 50ppm NO in N_2: The channel conductance decreases and increases instantaneously upon negative and positive gate bias application, followed by the gradual

increase and decrease in conductance during application of negative and positive gate voltages.

When a voltage is applied between the TFT gate and the source electrodes, a fraction of it falls across the gate dielectric while the remainder induces band bending within the semiconducting metal oxide (SMO) and corresponding band bending at the semiconductor metal oxide (SMO)/gas interface. For a sufficiently thin film, the effects of band bending induced at the SMO/gate dielectric interface is also observed at the SMO/gas interface.

Figure 31 illustrates the energy band diagram of TFT at equilibrium, E_F is constant, under oxidizing species such as O_2 and NO. Surface states created by chemisorbed species are represented as oval shaped band within the bandgap. When a positive gate bias $V_{GS} > V_{TH}$ is applied to the gate, electrons are accumulated in the semiconductor, reflected as an instantaneous increase in the channel conductance. Consequently, E_F instantaneously shifts upwards, leaving empty surface states below E_F. Then, induced electrons are trapped in these empty surface levels, acting as adsorption centers for oxidizing species[53]. As this field-induced adsorption takes places, i.e. while the gate bias is maintained at positive bias, the channel conductance ($G^t{}_{Vgs>0V}$) gradually decreases over time. As shown in figure 32(b), the surface potential V_s and E_s^- are increased as a result of the field-induced adsorption. Therefore, once the positive bias is removed from the gate, E_F lies farther from the conductance band E_C than it used to be, manifested as the increase in E_S^- and E_V^-, since the carrier concentration decrease after field-induced adsorption.

On the contrary, when the gate is biased negatively, hole concentrations are increased (electrons are depleted), exhibiting an instantaneous decrease in channel conductance. Accordingly, E_F of the semiconductor moves downwards. As shown in figure 33(a), the trapped electrons in the surface states recombine with the holes in the conduction band, causing the desorption of chemisorbed molecules. As the field-induced desorption occurs, i.e. while the gate bias is maintained at negative gate bias, the conductance ($G^t{}_{Vgs<0V}$) gradually increases over time. After the field-induced desorption is completed, both the surface potential V_S and E_S^- decrease (see figure 33(b)). The decrease in E_s^- also means that the E_F lies closer to the bottom of the conduction band, i.e. an decrease in the majority carrier concentration, as a result of the field-induced desorption.

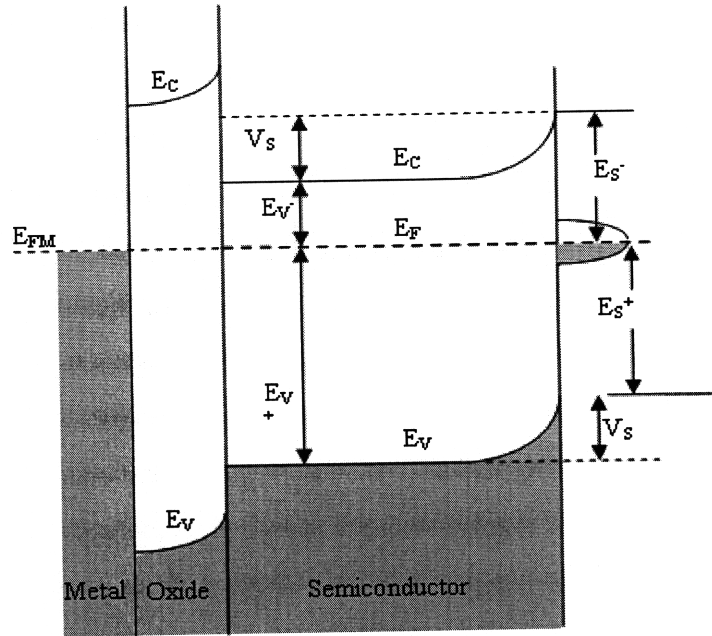

Figure 30. A schematic of an energy band diagram of TFT exposed to oxidizing gases.

Another feature in conductance changes, observed in figure 25, 26 and 27, should be clarified. After the removal of positive and negative gate voltages, TFTs exhibit similar conductance changes as if they are under negative or positive gate bias application, respectively, even though they are under zero gate bias. For example, the instantaneous increase in the channel conductance upon the removal of negative gate voltages, is followed by the gradual decrease in conductance during zero gate voltage application (see figure 25, 26 and 27), which is the same behavior to the ones observed while TFTs are under the influence of positive gate biases. This can be explained as a field memory effect. That is, the relative changes in the E_F position after the field induced chemisorption biases may serve as imaginary gate voltages. For instance, E_F under zero gate bias, shifted upwards as a result of field-induced desorption (negative gate voltages application), act as if it is raised by the positive gate voltage application. The reverse is true for field-induced adsorption (positive gate voltages).

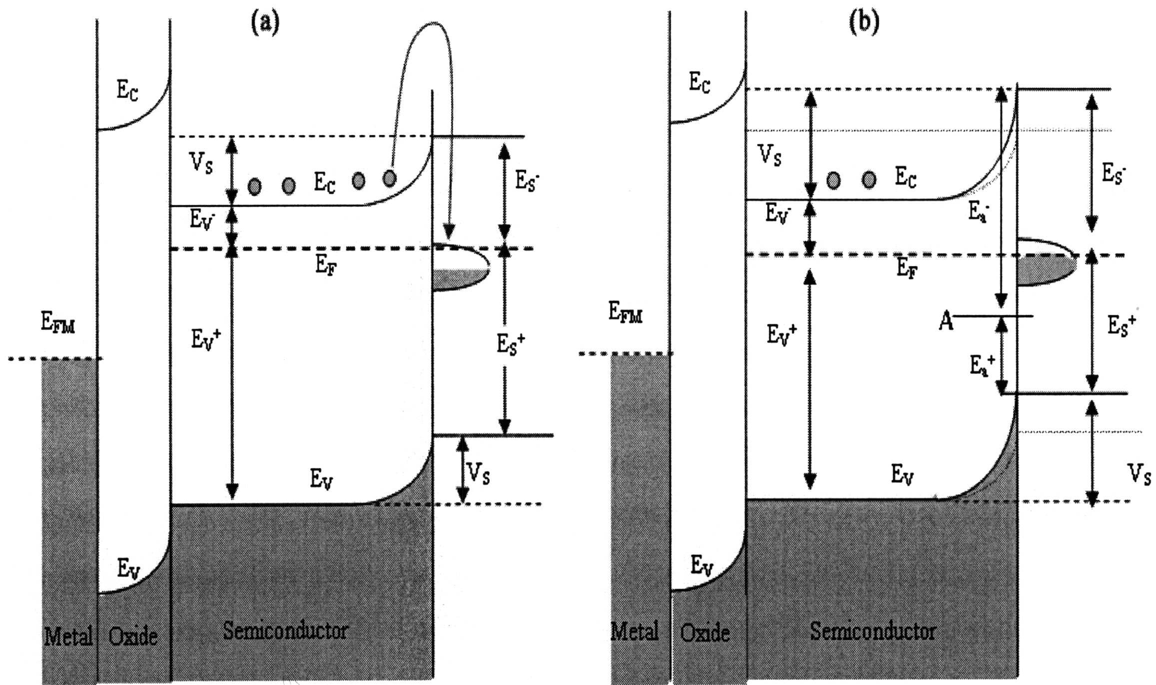

Figure 31. Schematics of energy band diagram during field-induced adsorption. TFTs are (a) under positive gate bias $V_{GS} > V_{TH}$ (b) after field induced-adsorption. Circles represent electrons.

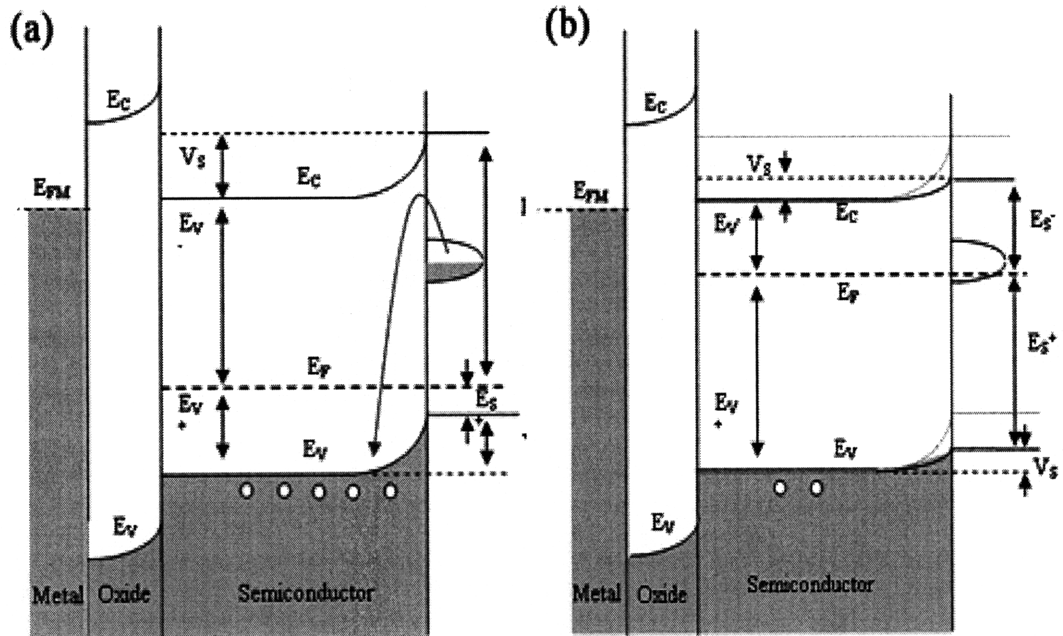

Figure 32. Schematics of energy band diagram of TFT during field induced-desorption. TFTs are under (a) negative gate bias and (b) after the field-induced desorption. Hollow circles represent holes.

To sum up, field-induced adsorption and desorption takes place when the n-type TFT is positively and negatively biased, respectively, under oxidizing environments such as O_2 and NO. This is manifested as a change in channel conductance at 0 V ($Gv_{gs=0V}$), an indicator of the carrier concentration in the IGZO film, as shown in figure 25, 26 and 27: the conductance at 0V ($Gv_{gs=0V}$) increases after successive application of negative gate biases, implying field-induced desorption of chemisorbed molecules. The opposite is true for successive application of positive gate biases. Furthermore, this conductance change is pronounced under the presence of oxygen molecules than that under high vacuum since only a very small number of molecules will be involved in the field-induced chemisorption under high vacuum.

These observations are consistent with the Volkenstein model presented earlier in section 2.3. Based on the Volkenstein model, the adsorption capacity of the metal oxide semiconductor, defined as the total number of chemisorbed species N, is related to the position of the Fermi energy E_F[54,55] by equation (2.11) given below (For detailed definition of each term, see the section 2.3). That is, by shifting E_F to higher or lower levels within the known energy landscape, surface states will populate or depopulate, depending on whether E_F lies respectively above or below the states.

$$N = N^0 + N^{\mp} = N^0[1 + \exp\left(\frac{E_a^{\mp} - E_s^{\mp}}{kT}\right)] \quad where \quad E_s^{\mp} = E_v^{\mp} + V_s \qquad (2.11)$$

For example, upon positive gate voltage application, E_F instantaneously shifts upwards, reflected as an increase in carrier concentration, causing a decrease in E_V^- and E_S^- (see figure 27). Accordingly, chemisorptive capacity N increases which means so does the field induced adsorption (see equation (2.11). Eventually, after the removal of the positive gate voltage, carrier concentration decreases, i.e. E_F decreases, and surface potential becomes higher than it was before.

Threshold voltage measurements, presented in section 4.3.1, can be easily understood based on the previous discussion about the influence of external electric field on chemisorption. Threshold voltage V_{TH} is measured, under 100 ppm NO in N_2 gas at room temperature, immediately following the removal of the gate bias which had been

maintained previously for a fixed period of time. As shown in figure 25, V_{TH} decreased after successively higher negative gate biases and partially recovered after applying 0 volts for 3 hours. On the other hand, V_{TH} increased with successively higher positive gate biases. Taking into consideration that a decrease in V_{TH} indicates an increase of carrier concentration, i.e. increase in the E_F, in the IGZO film, and vice versa, this result can be attributed to field-induced desorption and adsorption for negative and positive gate biases, respectively. Given that NO, a strong oxidizing gas, usually requires thermal energy to desorb from the semiconducting metal oxide (SMO), this result strongly suggests that gate bias can indeed serve as a powerful tool for desorbing NO even at room temperature.

Table 7. Applied gate voltages and its effect on chemisorption (see figure 27)

	Chemisorption	**Transient effect**	**Permanent effect**
Positive (+) gate voltage	Field-induced adsorption	Carrier concentration↑ E_F↑(E_V^-, E_S^-↓) Chemisorptive capacity N↑	Carrier concentration ↓ E_F↓(E_V^-, E_S^-↑) V_S ↑ V_{TH}↑
Negative (-) gate voltage	Field-induced desorption	Carrier concentration ↓ E_F↓(E_V^-, E_S^-↑) Chemisorptive capacity N↓	Carrier concentration↑ E_F↑(E_V^-, E_S^-↓) V_S ↓

Lastly, time constants for field-induced desorption are obtained as a function of temperature to confirm that observed conductance changes are due to chemisorptive

processes. As summarized in Table 4, desorption kinetics are enhanced, i.e. time constants become smaller, as the operation temperature increases upon negative gate bias application under the 50ppm NO/N_2 environment. Furthermore, the previously mentioned field memory effect, i.e. re-adsorption of NO even under zero gate bias, also exhibits temperature-dependent behavior; the higher the temperature, the faster the re-adsorption of NO resulting from the field effect.

Similar studies performed on ZnO[48] reported that application of positive and negative biases caused corresponding oxygen adsorption and desorption, respectively, measured with a mass spectrometer, under the partial pressure of oxygen 10^{-2} torr at 170^{0}C. However, Wöllenstein *et. al.*, observed increased sensitivity when a SnO_2 TFT was exposed to NO_2 gas under the influence of negative gate bias at 300^{0}C. They argued that a negative gate bias induces electron accumulation in the semiconductor, eventually leading to increased adsorption of the oxidizing gas. Measurements repeated with NH_3, a reducing gas, showed improved sensitivity under positive gate bias.

6. Summary and future work

Thin film semiconducting metal oxide (SMO) gas sensors are intensively studied given their high sensitivity, ability to be intergrated into microarrays and simple measurement and fabrication methods. However, thin film SMO gas sensors suffer from poor selectivity and slow chemisorption and desorption kinetics, high power consumption, and degradation. In this study, three approaches have been followed to improve kinetics; a new material, namely, $InGaZnO_4$, illumination and the field effect. Amorphous $InGaZnO_4$ has received intense attention owing to its high mobility (>10 $cmV^{-1}s^{-1}$) and compatibility with low temperature processing. However, most of the studies focus on its use as a transparent thin film transistor, a switching device for pixels in active matrix liquid crystal displays (AMLCDs). In this study, $InGaZnO_4$ was investigated as a promising candidate for semiconducting metal oxide (SMO) gas sensors operating at reduced temperatures. Fast adsorption kinetics of NO_2 are observed at room temperature and activation energies for oxygen and NO_2 were extracted as 0.07 and 0.19eV, respectively. A second approach investigated in this thesis to enhance sensor kinetics was the reduced temperature photo-

induced desorption of O_2 and NO_2 from IGZO thin films. Lastly, the influence of the application of an electric field on chemisorption and desorption was examined in thin film transistor (TFT) structures. TFTs offer the opportunity to readily control band bending at the SMO/gas interfaces via the gate voltage. Negative and positive gate voltages were confirmed to induce corresponding desorption and chemisorption of oxidizing gases such as O_2 and NO.

While most theories on semiconducting metal oxides are based on polycrystalline films, modeling of this amorphous oxide semiconductor, IGZO, should be simplified given the lack of grain boundaries and their often complex influence on sensor response. Along with modeling, the adsorption and desorption kinetics of IGZO thin films should be examined within small volume chambers which would allow for a direct examination of sensor response times and thereby a more reliable opportunity to examine the underlying kinetics. The Volkenstein model describes the basis of the mechanism underlying the field induced desorption and chemisorption in semiconductors by relating E_F and the chemisorptive capacity of semiconductor films. Additional modeling is needed to extend the Volkenstein model to very thin films as \found in TFTs.

Other suggested studies include (1) extension of sensor performance studies to a wider range of concentrations, (2) photodesorption and photoadsorption studies as a function of illumination intensity and wavelength under various gaseous atmospheres , (3) investigating field induced chemisorption as a function of the initial annealed state, temperature, and concentration of analytes, (4) comparison of sensor performance and kinetics between amorphous and single crystalline IGZO, (5) investigating the role of composition of IGZO film in influencing sensor response.

References

[1] K. Oto, A. Shinobe, M. Manabe, H. Kakuuchi, Y. Yoshida and T. Nakahara, New semiconductor type gas sensor for air quality control in automobile cabin, Sens. Actuators B 77 (2001) 525-528.

[2] S. N. Malchenko, I. N. Lychkovsky and M. V. Baykov, One-electrode semiconductor sensors for detection of toxic and explosive gases in air, Sens. Actuators B 7 (1992) 505.

[3] D. Kohl, J. Phys. D: Appl. Phys. 34 (2001) R125.

[4] N. Funazaki, A. Hemmi, S. Ito, Y. Asano, Y. Yano, N. Miura and N. Yamazoe, Application of semiconductor gas sensor to quality control of meat freshness in food industry, Sens. Actuators B 25 (1995) 797.

[5] L. T. Di Benedetto, P. W. Alexander and D. B. Hibbert, Portable battery-powered flow injection analyser for volatile alcohols using semiconductor gas sensors, Anal. Chimica Acta, 321 (1996) 61.

[6] E. Schaller, J. O. Bosset and F. Escher, 'Electronic noses' and their application to food, Lebensm.-Wiss.u.-Technol., 31 (1998) 305.

[7] T. Bachinger and C.-F. Mandenius, Searching for process information in the aroma of cell cultures , Trends Biotechnol. 18 (2000) 494.

[8] S. Ehrmann, J. Jüngst, J. Goschnick and D. Everhard, Application of a gas sensor microarray to human breath analysis, Sens. Actuators, B 65 (2000) 247.

[9] P. T. Moseley, Solid state gas sensors, Meas. Sci. Technol., 8 (1997) 223-237

[10] K. J. Albert, N. S. Lewis, C. L. Schauer, G. A. Sotzing, S. E.Stitze, T. P.Vaid, and D. R.Walt, Cross-Reactive Chemical Sensor Arrays, Chem. Rev. 100 (2000) 2595.

[11] K. Wiesner, H. Knözinger, M. Fleischer, and H. Meixner, Working mechanism of an ethanol filter for selective high-temperature methane gas sensors, IEEE Sensors J., 2 (2002) 354.

[12] Donghun Kang, Hyuck Lim, Changjung Kim Ihun Song, Amorphous gallium indium zinc oxide thin film transistors: Sensitive to oxygen molecules. Appl. Phys.Lett., 90, (2007) 192101.

[13] J.Lagowski, E.S. Sproles,Jr.,and H.C. Gatos, Quantitative study of the charge transfer in chemisorption; oxygen chemisorption on ZnO, J.Appl. Phys.,48 (1977) 3566

[14] W. Hellmich, G. Muller a, Ch. Bosch-v. Braunmuhl, T. Doll , I. Eisele , Field-effect-induced gas sensitivity changes in metal oxides ,Sensors and Actuators B, 43 (1997) 132

[15] J. Dalin, Final thesis Linköpings Institute of Technology, Sweden, 2002.

[16] Yong Ki Min, Properties and Sensor performance of Zinc Oxide Thin Film, Ph.D thesis, Department of Materials Science and Engineering, MIT,, 2003.

[17] N. Barsan and U. Weimar, Conduction model of metal oxide gas sensors, J. Electroceramics, 7 (2001) 143.

[18] G.Korotcenkov, Metal oxides for solid-state gas sensors: What determines our choice? Materials Science and Engineering B, 139 (2007) 1-23

[19] P.T. Mosely and B.C. Tofield, Solid State Gas Sensor, Adam Hilger, Bristol and Philadelphia, 1987

[20] H.L. Tuller and R. Mlcak, Advanced sensor technology based on oxide thin film-MEMS integration, Journal of Electroceramics, 4 (2000) 415-425

[21] I.-D. Kim, A. Rothschild, T. Hyodo, and H. L. Tuller, Nano Lett., 6 (2006) 193-198.

[22] Kagan, Andry, Thin-film transistors,, Marcel Dekker, Inc, 2003,.p.71.

[23] R.E.I.Schropp et al, New challenges in thin film transistor (TFT) research, J.Non-crystalline Solids 299-302 (2002) 1304-1310.

[24] S D Brotherton, Polycrystallin silicon thin film transistors, Semicond. Sci. Technol., 10 (1995) 721-738

[25] Y. Kuo, Thin film transistors : materials and processes, Kluwer Academic Publishers (2004)

[26] G. Horowitz, Organic field-effect transistors , Adv. Mat., 10 (1998) 365-377,.

[27] P. K. Weimer, The TFT-A new thin film transistor, Proc. IRE, June (1962)

[28] David W.Greve, Field effect devices and applications, Prentice hall, 1998, p.280-282.

[29] F.F.Volkenshtein, Electronic processes at the surface of a semiconductor during chemisorption, Soviet physics uspekhi, Vol 9, N0.5 (1967)

[30] W.E.Spear, P.G. LeComber, Substitutional doping of amorphous silicon, Solid State Commun. 17 (1975) 1193

[31] O. Hiromichi, H. Hosono, Transparent oxide optoelectronics, Materials Today, 7, (2004), 42-51.

[32] G. Thomas, Invisible circuits, Nature, Vol. 389.2004,907-908

[33] H. Kawazoe, M. Yasukawa, H. Hyodo, M. Kurita, H. Yangai, H. Hosono, P-type electrical conduction in transparent thin films of $CuAlO_2$, Nature, 389, (1997) 939-942.

[34] H. Hosono, Ionic amorphous oxide semiconductors: Material design, carrier transport, and device application, J. of Non-crystalline Sol. 352 (2006) 851-858

[35] K.Nomura, H.Ohta, A. Takagi, T. Kamiya, M. Hirano, H. Hosono, Room temperature fabrication of transparent flexible thin- film transistors using amorphous oxide semiconductors, Nature (2004) 488-492

[36] H. Hosono, K.Nomura , Factors controlling electron transport properties in transparent amorphous oxide semiconductors, J. of Non-Crystalline Solids 354 (2008) 2796-2800

[37] H. Kumomi, Amorphous oxide channel TFTs, Thin Sold Films, (2007)

[38] A. Takagi, K. Nomura, Carrier transport and electronic structure in amorphous oxide semiconductor, a-$InGaZnO_4$, Thin Solid Films 486 (2005) 38-41

[39] K. Nomura,Local coordination structure and electronic structure of the large electron mobility amorphous oxide semiconductor In-Ga-Zn-O: Experiment and ab initio calculations, Phys. Rev. B 75

(2007) 035212.

[40] K. Nomura , Subgap states in transparent amorphous oxide semiconductor, In-Ga-Zn-O, observed by bulk sensitive x-ray photoelectron spectroscopy, Appl. Phys. Lett. 92, (2008) 202117.

[41] T. Kamiya, H. Hosono, Electronic structure and device applications of transparent oxide semiconductors: What is the real merit of oxide semiconductors? Int. J. Appl. Ceram.Tech., 2 (2005) 285-294.

[42] H. Hosono, Recent progress in transparent oxide semiconductors: Materials and device application, Thin solid films 515(2007) 6000-6014.

[43] E. Comini, A. Cristalli, C. Faglia, and G. Sberveglieri, Light enhanced gas sensing properties of indium oxide and tin oxide sensors, Sens. Actuators B 65 (2000) 260.

[44] E. Comini, G. Faglia and G. Sberveglieri, UV light activation of tin oxide thin films for NO_2 sensing at low temperatuere, Sens. Actuators B 78 (2001) 73.

[45] E. Comini, L. Ottini, G. Faglia, and G. Sberveglieri, SnO_2 RGTO UV activation for CO monitoring , IEEE Sensors J. 4 (2004) 17.

[46] K. Anothainart, M. Burgmair, A. Karthigeyan, M. Zimmer, and I. Eisele, Light enhanced NO_2 gas sensing with tin oxide at room temperature: conductance and work function measurements, Sens. Actuators B 93 (2003) 580.

[47] X.Y.Zhu, Surface photochemistry, Annu. Rev. Phys. Chem. 45 (1994) 113-44.

[48] A. A. Lisachenko, Photon-driven electron and atomic processes on solid-state surface in photoactivated spectroscopy and photocatalysis, J. of Photochem. and photobiology A: Chemistry 196 (2008) 127-137.

[49] Z. L. Wang, Zinc oxide nanostructures: growth,properties and applications, J. Phys: Condens. Matter, 16 (2004) R829-R858

[50] D.H. Zhang, D.E. Brodie, Photoresponse of polycrystalline ZnO films deposited by r.f. bias sputtering, Thin Solid Film 261 (1995) 334-339

[51] D.H. Zhang, Adsorption and photodesorption of oxygen on the surface and crystallite interfaces of sputtered ZnO films, Materials Chem. and Phys. 45 (1996) 248-252.

[52] M. Takeuchi, K. Inoue, Photoconductive properties of ultrafine indium oxide particle layers, Applied Surface Science 33/34 (1988) 905-912

[53] V.G. Devyatov , Influence of external electric field on oxygen and carbon monoxide adsorption, React, Kinet, Catal. Lett., 9, (1978) 199-204

[54] F.F. Volkenshtein, The Electronic Theory of Catalysis on Semicoductors, The Macmillan Company, New York, 1963.

[55] H. Geistlinger, Electron theory of thin-film gas sensors, Sensors and Actuators B17 (1993) 47-60.